The Pennsylvania State University

The Graduate School

Department of Electrical Engineering

AIRBORNE PARTICULATE MATTER IN THE URBAN ENVIRONMENT DURING SUMMER IN THE NORTHEAST UNITED STATES

A Thesis in

Electrical Engineering

by

Greggory L. O'Marr

Submitted in Partial Fulfillment
of the Requirements
for the Degree of

Master of Science

May 2002

Greggory L. O'Marr

We approve the thesis of Greggory L. O'Marr.

Date of Signature

C. Russell Philbrick
Professor of Electrical Engineering
Thesis Advisor

Sven Bilén
Assistant Professor of Electrical Engineering

W. Kenneth Jenkins
Professor of Electrical Engineering
Head of the Department of Electrical Engineering

ABSTRACT

Laser remote sensing techniques have been used to investigate atmospheric optical characteristics and to provide a means of describing the effects of local air pollution events. The North American Research Strategy for Tropospheric Ozone – North East – Oxidant and Particle Study (NARSTO-NE-OPS) study conducted in an urban area of Philadelphia, U.S. provided a chance to apply several of Penn State University's LIDAR instruments to investigate optical properties of the lower troposphere. The Lidar Atmospheric Profile Sensor (LAPS) unit measured ozone, water vapor, temperature, direct backscatter, and extinction; the Micro Pulse Lidar (MPL) measured backscatter; and the Multistatic Atmospheric Particle Profiler (MAPP) measured intensity from an off-axis angle and estimated particle size distribution. Analysis of data from several days during three field research campaigns are used to show how remote sensing can be used to characterize atmospheric aerosols for pollution modeling. Direct backscatter profiles distinguish areas of strong signal return from regions of dense concentrations of aerosols, such as clouds, mist, fog, or haze. Pollution and haze events demonstrate the capabilities of lidar to characterize optical properties of atmospheric aerosols. Comparisons of water vapor and extinction plots from 19-22 August 1998 show convection within the lower troposphere as the planetary boundary layer expands after sunrise and aerosols mix downward from a higher altitude layer. The 284-nm extinction profiles from 07 August 1999 and 12 August 1999 show small diameter aerosols distributed within the lower troposphere, since shorter wavelengths

scatter more from small particles due to λ^{-4} dependence; while 530-nm extinction profiles display higher altitude clouds. These comparisons, between two transmitted wavelengths, allow aerosol mode estimates to be made. Lidar data from 16-17 August 1999 show how Philadelphia was affected by a northeast coastal haze event that extended from the Chesapeake Bay to Maine. Ultrafine aerosols are mixed from 0-2 km while fine and large mode aerosols form a ground layer between 0-250 m. MAPP images on 23 August 2001 display two distinct aerosol layers within the first 40 m of the atmosphere while 284- and 530-nm extinction plots show condensation growth of particles within the first 100 m of the atmosphere.

TABLE OF CONTENTS

LIST OF FIGURES

LIST OF TABLES

ACKNOWLEDGMENTS

I would like to thank my advisor, Professor C.R. Philbrick, for his support and guidance through my research and academics. I would also like to thank Dr. Sven Bilén for his support and guidance through my academics and the Get Away Special Project.

Thanks are also due to Tom Petach, Edie S. Sears, , Alex Achey, Guankum Li (Homer), Ginnipal Chada, Sriram Kizhakkemadam, Steve Esposito, Karoline R. Mulik, Gioia Massa, Micheal Wyland, Linda Becker, and Diana Feltenberger. I would especially like to thank Edward J. Novitsky for is help and guidance during the research and writing processes of my thesis and for blazing a path first.

I would like to thank my family and friends for their encouragement and understanding. Their love and support helped me throughout my studies and encouraged me to achieve my goals. I would also like to thank Mr. Ward, Mrs. Peckham, Mr. Seiler, Mr. Ebersbach, and Mrs. Knowles for instilling a desire to pursue math and science and to do the best that I can.

I would like to thank Dr. Richard Clark of Millersville University and the Harvard University – School of Public Health for the use of their data. I acknowledge the support of my graduate research by the United States Environmental Protection Agency, grant # R826373.

Chapter 1

Introduction

This thesis will explain several laser remote sensing instruments used by researchers at the Penn State University Lidar Laboratory and the optical scattering principles they use. Atmospheric profiles of extinction, optical scattering, and water vapor will be described to better understand processes involved in formation, transport, and loss of aerosols. Data taken during several field research campaigns will be presented, analyzed, and compared. Pollution and haze events will be used to demonstrate the capabilities of lidar to characterize optical properties of atmospheric aerosols. Time-sequenced water-vapor ratio plots show the result of convective mixing and clearly define the planetary boundary layer. Atmospheric optical extinction at two wavelengths, UV and visible, will be used to estimate aerosol mode ranges [Schuster et al., 1998]. The use of multi-wavelength scattering by aerosols can provide information on aerosol mode ranges, layers, convection and advection in the lower troposphere. Multistatic Atmospheric Particle Profiler (MAPP) snapshots of the lower troposphere will show aerosol layers from 0-100 m. Data from tethered balloons and ground-based particle-sizer instruments will be used to develop arguments, which support interpretations of the lidar data.

Multiple lidar instruments were operated simultaneously during summer campaigns in 1998, 1999 and 2001, to take vertical profiles providing aerosol and meteorological data. Profiling and modeling of airborne aerosols within the atmosphere

(especially in the lower troposphere) by making use of their optical scattering properties, provides an important input for studying the sources and sinks of the aerosols. This includes investigations of how the aerosols are transported, how they react with chemical species and with other aerosols, and how they respond to meteorological conditions. By using their optical properties, the physical and chemical processes of the aerosols associated with air pollution episodes can be modeled and refined. The lower troposphere (from the ground to about 2 km) is the region that has the greatest impact upon people and it is the region most affected by human activity. Aerosol studies are important because aerosols have been shown to affect human health, local and global climate, and visibility.

Vertical profiles of atmospheric properties using laser remote sensing techniques provide an important contribution to investigations of physical and chemical processes. Since a continuous time sequence atmospheric cross-section can be made from vertical profiles, the atmospheric variations can be studied from the ground through the lower atmosphere as they are advected past the site. Most other data gathering methods for the atmosphere, such as sounding rockets, airplanes, tethered balloons, or meteorological towers, only provide *in situ* measurements at one altitude at a time. Sounding rockets and balloon sondes can provide a profile measurement but require time for launching and have significant costs associated with expendable hardware. Also, unlike these other methods, laser remote sensing instruments can also be continuously run with limited human monitoring.

Chapter 2

Lidar Instruments and Measurement Techniques

2.1 Introduction

Lidar (LIght Detection and Ranging) is a remote sensing technique used to profile the constituents and properties of the atmosphere. Data profiles have been obtained by *in situ* measurements on balloons, aircraft, or rockets, but these methods are costly and may provide only a single profile. Lidar instruments use a laser transmitter and receive a signal from the optical scattering of the transmitted beam by molecules and particles to provide the primary data. The short pulse of a laser transmitter is timed from transmission to reception to assign an altitude to the measurements. Balloons, aircraft, and rockets provide only *in situ* point measurements; lidar instruments provide continuous profiles of the parameters.

2.2 Scattering Signals

Lidar instruments use a laser as their transmitter source and allow a range of specific frequencies in the UV-to-IR spectrum to be selected. A laser transmits a polarized beam with an intensity cross-section of a Gaussian amplified distribution centered at the desired wavelength [Hecht, 1997]. When the transmitted laser photon interacts with a particle in the atmosphere, it will either be absorbed if the atom or

molecule has an energy level near the transmitted wavelength, or the photon will be scattered by producing a virtual energy state that corresponds to the photon energy and then be instantly reemitted. The process of scattering can occur as an elastic or inelastic event due to the presence of vibrational and rotational energy states in the molecule or molecules composing the particle. Photon-particle scattering interaction will result in an angular distribution of scattered photon directions; however, the monostatic and multistatic lidar receiver units discussed in this thesis only collect photons at scattering angles of 145^{o} to 180^{o} to the beam direction. Optical wavelength scattering is dependent on the diameter of the particle relative to the scattering wavelength [Anthes et al., 1975]. There are several theories for calculating scattering processes of scattering, but we will only be considering three types: Rayleigh scattering, Mie scattering, and Raman scattering.

2.2.1 Rayleigh Scattering

When the particle diameter is very small compared to the wavelength (particle diameter less than $\lambda/15$), an incident electromagnetic wave that is scattered elastically from a dielectrically spherical particle is called Rayleigh scattering [Bohren and Huffman, 1983]. Elastic scattering means that as one photon is absorbed another one is instantly reemitted with the same frequency, see Figure 2.1. The transmitted wavelength is only modified slightly by Doppler shifting due to the thermal motion of the scattering molecule or particle. The particle can be viewed as a ground state oscillator, oscillating at the same frequency as the incident wave and reradiating the incident power as a dipole

radiation pattern [Bohren and Huffman, 1983]. The scattered intensity changes as the cross-section which depends on ω^4 ($1/\lambda^4$) and on r^6 as the frequency of the radiation and/or the size of the particle change [Measures, 1984].

Figure 2.1. Rayleigh scattering [Measures, 1984].

2.2.2 Mie Scattering

The scattering theory developed by Gustav Mie is a more general case that applies to the case of electromagnetic wave scattering from spherical scatterers of all sizes, and includes Rayleigh scattering as a special case when particles are small compared to the incident wavelength [Hecht, 1997]. Mie scattering theory is needed to describe the scattering from homogeneous spheres, see Figure 2.2. When a plane wave (laser beam) interacts with an array of atoms spherical wavelets are created (scattered), which form a secondary wave front. Optical wavelengths constructively scatter as wavelets from a spherical scattering particle, but as particle diameter increases the wavelets begin to destructively scatter [Hecht, 1997]. In effect, small diameter particles are more efficient scatters of shorter wavelengths, but as particle diameter increases so does the scattering of longer wavelengths.

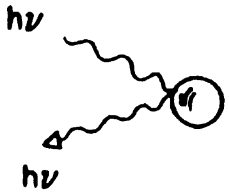

Figure 2.2. Mie scattering [Measures, 1984]. The incident photon's incident frequency remains unchanged from scattering.

2.2.3 Raman Scattering

Raman scattering includes the inelastic scattering processes when discrete energy quanta are removed from or added to the energy of an incident electromagnetic wave. The discrete energy levels associated with the vibrational and rotational states of the molecule or particle participate in changing the energy of the scattered photon. In an inelastic process, an incident photon is absorbed by a particle raising its energy level to a virtual state, and the particle instantly returns to a lower energy state with emission of a frequency-shifted photon, see Figure 2.3. Raman scattering can be related to Rayleigh scattering by the fact that an incident photon is modulated by molecular vibrations and rotations, which produce the Raman effect [Kyle, 1991]. The new photon will either have lost energy and be red-shifted (frequency loss), which is called a Stokes transition, or it will be blue-shifted (frequency gain), which is called an anti-Stokes transition [Measures, 1984]. These shifts are seen as side bands of the transmitted wavelength. The difference between the incident wavelength and the side bands is dependent on the particular molecules or particles involved [Hecht, 1997].

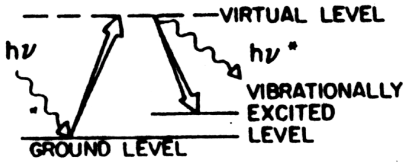

Figure 2.3. Raman scattering [Measures, 1984].

2.3 LIDAR Instruments

In the field of remote sensing there are several ways to implement a lidar instrument. The design of the device depends on what will be detected and where the parameter will be measured. The Penn State University Lidar Laboratory personnel have designed several lidar instruments, two of which will be discussed here. Also included will be an instrument fabricated by Science and Engineering Services, Inc. (SESI) and used occasionally by the Penn State University Lidar Laboratory.

2.3.1 Lidar Atmospheric Profile Sensor

The Penn State University Lidar Laboratory, in the Electrical Engineering Department, has developed several laser remote sensing instruments and uses a monostatic coaxial lidar system called LAPS (Lidar Atmospheric Profile Sensor) for many research tasks. LAPS was developed as a prototype lidar to provide profiles of RF refraction and meteorological properties for the United States Navy. The system consists of several subsystems including a laser transmitter, telescope receiver, optical wavelength detection box, photon counting electronics, and a control/processing computer. The

instrument makes use of vibrational and rotational Raman scattering techniques along with Rayleigh/Mie scattering theory to determine profiles of several atmospheric properties such as water vapor content and temperature. LAPS consists of two main components: the deck unit and the console unit. The deck unit houses the transmitting and receiving hardware, while the console unit houses the control/processing, detection, and photon counting hardware. The two units are connected via Ethernet cable for computer monitoring and control, and a fiber optic cable for transfer of the optical data signals from the receiving telescope to the detector subsystem. LAPS characteristics can be found in Table 2.1 [Philbrick and Mulik, 2000].

Table 2.1. LAPS summary

Laser transmitter	Continuum Model 9030 with 5X Beam Expander
Pulse Repetition Frequency	30 Hz
Pulse Duration	8 ns
Fundamental Power	1.6 J/Pulse
Power Output at 1064 nm	Dumped into heat sink
Power Output at 532 nm	600 mJ
Power Output at 266 nm	90 mJ
Telescope receiver	61-cm diameter parabolic mirror
Receiver signal transfer	All-Silica SFS fiber optic cable – 1 mm core
Detector box (8 channel)	660 and 607 nm - Water Vapor 528 and 530 nm - Temperature 295 and 284 nm - Daytime Water Vapor 277 and 284 nm - Raman/DIAL Ozone 607, 530 and 284 nm - Extinction 532 nm - Backscatter
Data system	DSP 100 MHz with 75-m range bins
Safety radar	Marine R-70 X-Band provides 6^{o} cone angle for beam

2.3.1.1 Deck Unit

The transmitter is a Continuum 9030 Nd:YAG laser with a fundamental wavelength of 1064 nm. Non-linear crystals are used to double the fundamental to 532 nm (2^{nd} harmonic) and then doubled again to 266 nm (4^{th} harmonic). The receiver consists of a 61-cm diameter parabolic telescope mirror with a 1.5-m focal length. A 1-mm diameter fiber optic cable is located just beyond the mirror's focal point. Receiver layout can be seen in Figure 2.4 [Jeness et al., 1997]. If the fiber is located at the focal point, it is at the mirror's infinity focus and the laser beam's blur circle (approximately 0.3 mm) will be smaller than the diameter of the fiber (1 mm). When the fiber is positioned slightly beyond the focal point the fiber will receive ray paths that are converging from near field and diverging after the far field focus [Jeness et al., 1997].

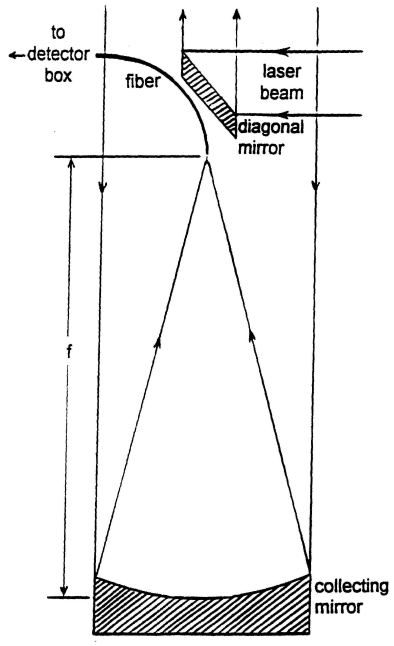

Figure 2.4. LAPS receiver setup [Jeness et al., 1997].

2.3.1.2 Console Unit

The scattered light signal, collected by the telescope and focused onto the end of a 1-mm diameter optical fiber cable, is transferred to the detector box that is attached to the back of the console. The optical signal diameter is expanded to a 1-cm beam diameter upon entry into the box. Beam splitting optics are used to separate the signal into 277, 284, 295, 528, 530, 532, 607, and 660 nm components, see Figure 2.5. A recent modification, which repaired an optical vignetting problem caused by the 532-nm beam splitter, required the removal of a beam splitter and the addition of a 45^{o} mirror for the direct backscatter channel [Chadha, 2001]. Narrowband filters are then used along with blocking filters, neutral density filters, and spot focusing lenses to condition the individual signals for each PMT (photomultiplier tube). The photon counting PMTs turn the optical signal (photons) into an electrical signal (current and voltage), which is then amplified and threshold detected by the counting electronics. Seven channels have a 75-m range resolution because of the fixed 500 ns bin width of the photon counting electronics while the eighth channel, which measures the direct backscatter, at 532 nm (PCount) has a 3-m range resolution [Mulik, 2000].

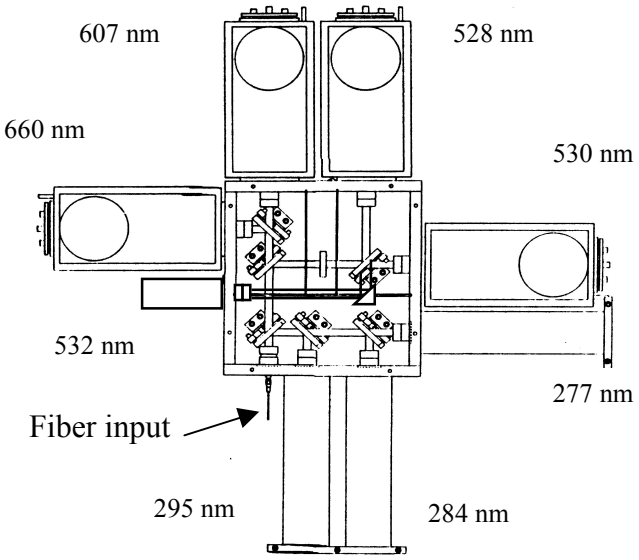

Figure 2.5. Detector box layout.

The console computer has a duel role in monitoring the deck unit and logging the received data signals. An Ethernet cable connects the console computer to the deck computer that controls the transmitting hardware. The console computer also does real-time processing of the incoming data and displays the data in several formats and plots for the operator to review.

2.3.2 Multistatic Atmospheric Particle Profiler

The Multistatic Atmospheric Particle Profiler (MAPP) instrument uses the LAPS laser for its transmitted signal and three digital cameras as receivers. The MAPP images the Rayleigh/Mie scattering to profile the molecular and particulate scattering properties, by taking the ratio of the parallel and perpendicular polarization phase functions over a range of scattering angles (145^o to 175^o) [Novitsky, 2002]. Meade Pictor 416XTE CCD

digital cameras were used to image backscatter intensity of the transmitted laser beam. Narrow band filters were used in front of each camera lens to isolate the 532-nm scattered signal. Each camera was connected via SCSI card to its own computer and the three computers were controlled by one computer through network connection. The cameras were set at specific distances from the vertically pointed laser so that their field of views would overlap and the laser beam infinity point was contained within the image, see Figure 2.6. A polarization rotator was used to change the transmitted laser beam's polarization between conditions of being parallel and perpendicular with respect to the measuring plane containing the cameras' and the beam, as shown in Figure 2.6. An imaging sequence was picked such that the images could be taken in under 2 minutes. Ideally the images for each polarization should be taken simultaneously but this would require two sets of equipment. The camera pixels that image the laser beam are integrated at each range in each image and used for the scattering analysis. The scattering data sets are input into scattering matrices and inverted to output the polarization ratio versus scattering angle, and polarization ratio versus altitude, (see Novitsky [2002] Chapters 3 and 6 for detailed explanations of the math and processing procedures involved).

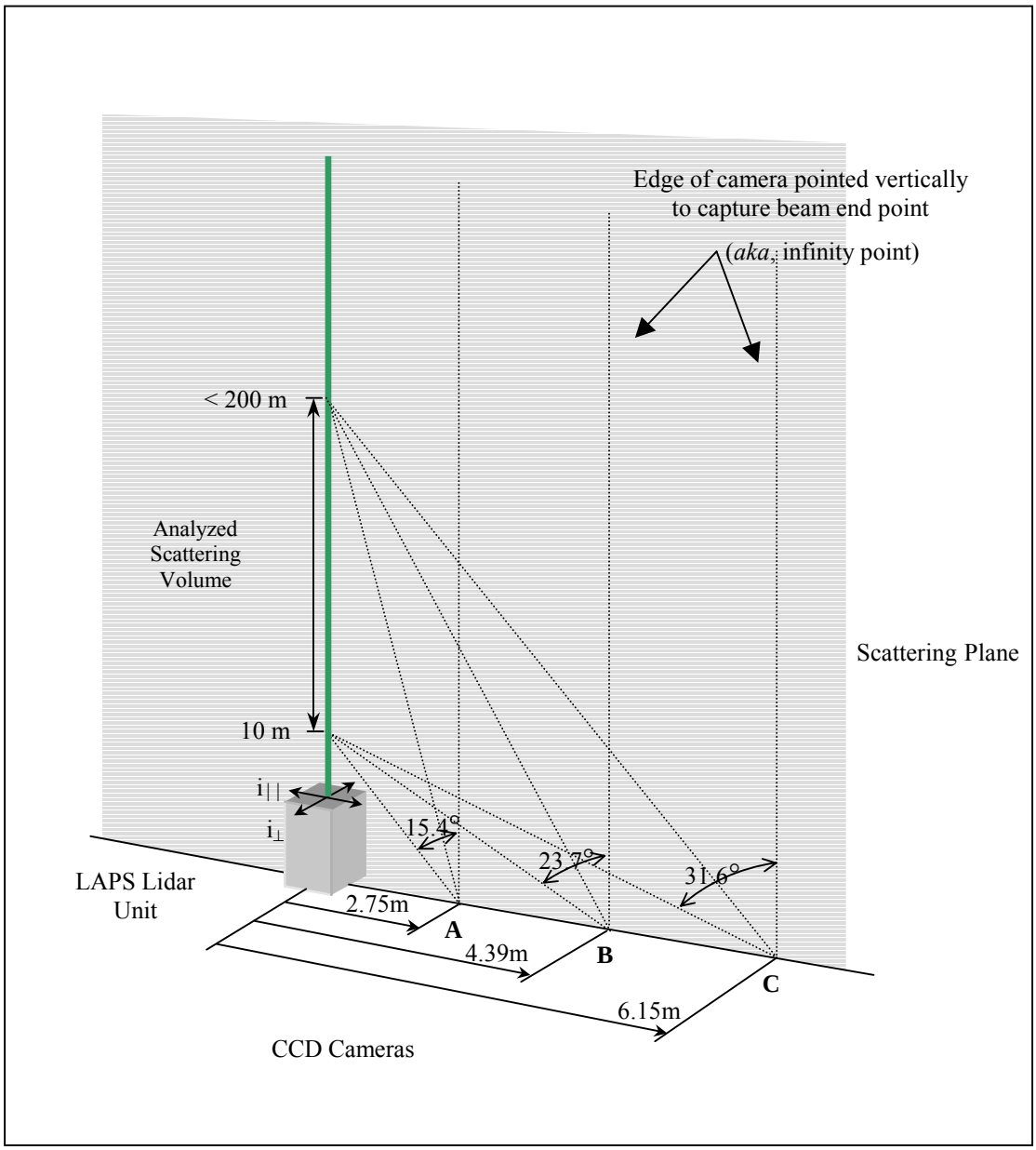

Figure 2.6. Multistatic equipment and configuration [Novitsky, 2002]

2.3.3 Micro Pulse Lidar

The Penn State Lidar laboratory has used the Micro Pulse Lidar (MPL) instruments, manufactured by Science and Engineering Services, Inc. (SESI), in several field studies. During the summer of 1998 NE-OPS campaign, the MPL Model 1000 Nd:YLF diode pumped laser (523 nm, 2nd harmonic) was used [Lee, 1996]. Table 2.2 contains the MPL instrument's characteristics. This model is a coaxially overlapped backscatter profiler and was operated in a vertical-pointed configuration to measure the molecular and particulate backscatter signal. By coaxially overlapped it is meant that the same telescope is used to transmit the laser and also used to receive the return signal. SESI provides a software package called WMPL to process and display data. However, a former student, Karoline Mulik, has written a MATLAB program for time-sequenced plotting that is used in this thesis. Plots display data collected in PhE/μs (TTL pulse counts/μs or photon counts/μs) [SESI, 1996]. See Mulik [2000]; Lee [1996]; Hlavka et al. [1998] or SESI [1996] for detailed reports that explain various details of the MPL instrument.

Table 2.2. MPL Characteristics [Mulik, 2000]

Detection Range	60 km
Altitude Resolution	30, 75, 150, and 300 m
Laser	Diode Pumped Nd:YLF
Wavelength	523.5 nm
Output Pulse Energy	10 μJ
Pulse Repetition Rate	1 to 10 kHz
Pulse Duration	10 ns
Telescope Diameter (Schmidt-Cassegrain)	0.2 m
Field of View	< 50 μrad
Detector	Geiger Mode Avalanche Photodiode
Bandwidth	0.2 nm

2.4 Measurement Techniques

The lidar instruments, LAPS, MAPP, and MPL, use the backscatter signals from a transmitted beam to determine properties of the atmosphere. The PCount channel of the LAPS instrument and the MPL measure Rayleigh/Mie scattering at 180^{o} to the transmitted direction, the MAPP measures the Mie scattering between the backscatter angles of 145^{o} to 175^{o}, and the seven main channels of LAPS measure the 180^{o} backscatter Raman signals. From these different types of signals, profiles of several properties can be obtained. Vertical profiles of optical scattering and extinction, due to molecules and particles will be the focus of this thesis and analysis techniques for Rayleigh scatter and Mie scatter theory will be applied.

2.4.1 Basic Lidar Equation

Vibrationally shifted Raman scatter signals are used to measure water vapor and optical extinction. These signals are generated during the process of scattering of the 532- and 266-nm transmitted laser beam from molecules in the lower troposphere. The 266 nm wavelength provides measurements during the day because it is in the "solar blind" region, while both the visible and ultraviolet channels are used at night. The 607 and 660 nm channels are used for the nighttime water vapor profiles, and the 607 and 530 nm signals are used for the nighttime optical extinction. The 295 and 284 nm signals are used for the day- and nighttime water vapor while the 284-nm profile provides the day- and nighttime optical extinction. The collected data can be analyzed to provide profiles

of the concentrations of N_2, O_2, and H_2O [Mulik, 2000]. The basic lidar scattering equation $P_{\lambda R}(z)$ is used to interpret the signal power photon counts for each species [Measures, 1984, Ansmann et al., 1992],

$$P_{\lambda R}(z) = K_{\lambda R} \frac{\xi(z)}{z^2} N(z) \frac{d\sigma}{d\Omega} \exp\left[-\int_0^z \left[\alpha_{\lambda T}^{\text{mol}}(z) + \alpha_{\lambda T}^{\text{aer}}(z) + \alpha_{\lambda R}^{\text{mol}}(z) + \alpha_{\lambda R}^{\text{aer}}(z) + \alpha_{\lambda T}^{\text{abs}}(z) + \alpha_{\lambda R}^{\text{abs}}(\xi) \right] d\xi \right], \quad [2.1]$$

where,

z	altitude of return signal scattering volume element,
λ_T	wavelength of transmitted signal,
λ_R	wavelength of received signal,
$K_{\lambda R}$	height independent system parameters,
$\xi(z)$	laser beam receiver field of view overlap function,
$N(z)$	molecular density profile,
$\frac{d\sigma}{d\Omega}$	range-independent differential Raman cross-section,
$\alpha_\lambda^{\text{mol}}$	extinction coefficient due to molecular components at λ,
$\alpha_\lambda^{\text{aer}}$	extinction coefficient due to aerosol components at λ,
$\alpha_\lambda^{\text{abs}}$	extinction coefficient due to optical absorption.

2.4.2 Water Vapor

A large portion of the atmospheric aerosol content is water vapor [Seinfeld and Pandis, 1998]. The water vapor content or mixing ratio (g/kg) is measured as a ratio of H_2O to N_2 in the atmosphere. Nitrogen is used as a constant and H_2O as the variable, since N_2 atmospheric content has been well studied and known. The water vapor mixing ratio, W, uses radiosonde balloon data to determine the *K* factor [Rajan et al., 1994],

$$W(z) = K \frac{S_{H_2O}(z)}{S_{N_2}(z)}, \qquad [2.2]$$

where,

S_{H2O}	signal received with Raman-shift of H_2O at 295 and 660 nm,
S_{N2}	signal received with Raman-shift of N_2 at 284 and 607 nm,
K	radiosonde calibration constant.

Due to the transmitted laser beam interaction with atmospheric constituents, Equation 2.2 must be augmented. Molecular scattering of the Raman-shifted 532-nm wavelength can be corrected for extinction due to the molecular scatter from O_2 and N_2 with Equation 2.3.

$$W(z) = K \frac{S_{H_2O}(z)}{S_{N_2}(z)} \exp(\sigma_{H_2O} - \sigma_{N_2}) K(z) \qquad [2.3]$$

where,

σ_{H2O}	Raman cross-section of H_2O at the transmitted wavelength,
σ_{N2}	Raman cross-section of N_2 at the transmitted wavelength,
$K(z)$	difference in molecular scattering, a known value.

The 266-nm transmission is within the Hartley band, where ozone (O_3) will absorb some of the laser and Raman scattered signals. By using the ratio of the Raman signals for O_2 and N_2, one can correct O_3 absorption influence on the water-vapor mixing-ratio Equation 2.4 [Esposito, 1999].

$$W(z) = K \frac{S_{H_2O}(z)}{S_{N_2}(z)} \left(\frac{S_{O_2}(z)}{S_{N_2}(z)} \right)^{\frac{\sigma_{H_2O} - \sigma_{N_2}}{\sigma_{N_2} - \sigma_{O_2}}} \qquad [2.4]$$

where,

S_{O2}	received Raman-shift of O_2 at 277 nm,
σ_{O2}	Raman cross-section of O_2 at the transmitted wavelength.

2.4.3 Extinction

Optical extinction in the atmosphere can be calculated directly by measuring the attenuation of a transmitted laser beam as it is scattered and absorbed by molecules and aerosols [Measures, 1984]. LAPS measures optical extinction at three wavelengths, 284, 530 and 607 nm. Each wavelength will have a different relative response for a different size range of the particulate distribution. The Raman-shifted vibrational nitrogen signals at 284 and 607 nm and the rotational Raman-shifted signal at 530-nm provide profiles that are proportional to density, except for loss due to scattering be molecules and particles [Philbrick, 1998]. Aerosol extinction is calculated by using the Beer-Lambert Law and describes the difference between the actual profile gradient and that expected from the molecular nitrogen density scale height, corrected for the molecular extinction path through the atmosphere. The total extinction within the atmosphere due to scattering and absorption by molecules and aerosols can be calculated by inverting the basic lidar equation,

$$\alpha^{\text{total}}(\lambda_R) = \frac{\dfrac{d}{dz}\left[\ln\left(\dfrac{N_R(z)}{P_{\lambda R}(z)z^2}\right) - \alpha_{\lambda T}^{\text{mol}}(z) - \alpha_{\lambda R}^{\text{mol}}(z) - \alpha_{\lambda T}^{\text{abs}}(z) - \alpha_{\lambda R}^{\text{abs}}(z)\right]}{1 + \left(\dfrac{\lambda_T}{\lambda_R}\right)^k}, \qquad [2.5]$$

where,

λ_T	transmitted laser wavelength,
λ_R	received laser wavelength,
$N_R(z)$	nitrogen molecule number density,
$P_{\lambda R}(z)$	power of the received wavelength from altitude (z),
$\alpha_\lambda^{\text{mol}}(z)$	extinction coefficient due to molecular components,
$\alpha_\lambda^{\text{abs}}(z)$	extinction coefficient due to optical absorption,

k	k~1 for aerosols and water droplets with diameters comparable to the measuring wavelength.

Extinction from absorption by molecules and particles is negligible at 530 nm. Also, the extinction from molecular scattering can be estimated from the surface pressure and rotational-Raman temperature profile. These factors leave the aerosol scattering as the only unknown, which can now be solved [Measures, 1984].

2.4.4 Direct Backscatter

Backscatter measurements made by the PCount and MPL are from the molecular and aerosol scattering of the LAPS instrument's transmitted 532-nm wavelength, and the MPL instrument's transmitted 523-nm wavelength, respectively. The backscatter lidar equation can be used to calculate the backscatter coefficient from the scattering cross-section of particles in the atmosphere [Measures, 1984],

$$\beta(\lambda, z) = \sum_i N_i(z) \left\{ \frac{d\sigma(\lambda, \theta = \pi)}{d\Omega} \right\}_i^S , \qquad [2.6]$$

where,

$N_i(z)$	number density of scattering species i at altitude z,
$\left\{ \frac{d\sigma(\lambda, \theta = \pi)}{d\Omega} \right\}_i^S$	differential scattering cross-section of species i.

Backscatter, like extinction, also depends upon on atmospheric aerosol size distribution. When aerosols reach a critical size, the ratio between backscatter and extinction will become constant.

2.4.5 Angular Scattering

By using Mie scattering of particles within the transmitted 532 nm laser beam volume a polarization ratio from the scattered phase functions over a spread of angles may be obtained. The MAPP instrument is a multistatic receiver uses a receiver and transmitter that are widely separated. The image data contains the intensity distribution of the scattered phase functions of a particular polarization (parallel or perpendicular) oriented to the digital camera imaging plane. The parameters of the lognormal distribution, N(r), representing the airborne aerosols may be deduced from the polarization ratio resulting from dividing the perpendicular with parallel image data [Novitsky, 2002]. By using the MAPP this distribution can be obtained for a range of altitudes.

To allow this approach to be useful and the collected data easily analyzed, several assumptions must be made. Aerosols or molecules within the scattering volume are assumed to be dielectric spheres with negligible imaginary indexes of refraction. Calculations of the scattering properties using Mie theory show that the polarization ratio in insensitive to imaginary indexes of refraction, on the order of 10^{-3}-10^{-8}; therefore, only the real component of the index of refraction will be considered [Novitsky, 2002].

The polarization ratio is then given by [Novitsky, 2002]:

$$PR(\theta) = \frac{I_{\text{Total}_{\parallel}}(\theta)}{I_{\text{Total}_{\perp}}(\theta)} = \frac{\int \left|S_2(r,\theta)\right|^2 y(r)dr + Molecular_{\parallel}}{\int \left|S_1(r,\theta)\right|^2 y(r)dr + Molecular_{\perp}}, \qquad [2.7]$$

where,

$I_{\text{Total}\parallel}(\theta)$ total scattering intensity from incident parallel polarization,

$I_{\text{Total}\perp}(\theta)$	total scattering intensity from incident perpendicular polarization,
$\left\|S_{1,2}(r,\theta)\right\|^2$	pre-calculated scattering matrices (for given wavelength and index of refraction)
$y(r)$	total lognormal number density distribution (#/m^3 versus particle radius),
$Molecular_{\perp\|\|}$	molecular scattering components at each polarization.

This calculation will give the polarization ratio for all particles within a given altitude range. For a detailed explanation of the theory and design of the MAPP instrument see Novitsky [2002].

Chapter 3

Aerosol Effects on Climate, Visibility, and Health

3.1 Introduction

Air pollution has been shown to have dramatic health effects for the two extremes of the human age spectrum, the young and the elderly. It also affects a region's visual aesthetics, i.e., air pollution causes increased optical extinction, leading to visual range reduction [EPA, 2002a; Seinfeld and Pandis, 1998]. However, to understand and analyze aerosols one must know how they are contributing to these concerns.

3.2 Aerosols

An aerosol is a solid or liquid particulate in a gas [Seinfeld and Pandis, 1998]. This means an aerosol can be a solid particle, liquid droplet or a solid particle encapsulated by a liquid.

3.2.1 Classification

Aerosols are divided into two categories based on how they are entrained in the atmosphere: primary aerosols, which enter the atmosphere directly through human or meteorological processes, and secondary aerosols which result from gas-to-particle

conversions within the atmosphere [Seinfeld and Pandis, 1998]. The primary and secondary groups are further subdivided based on size and production mechanism, which are summarized in Table 3.1 [Seinfeld and Pandis, 1998].

Table 3.1. Aerosol classification by size and cause of production [Seinfeld and Pandis, 1998]

Name	Mode	Primary Formation	Size Range
Ultrafine or Aitken Nuclei	Nucleation	Gas-to-particle	0.001-0.1 μm
Fine or Large	Accumulation	Coagulation	0.1-2.5 μm
Coarse or Giant	Coarse	Mechanical	<2.5 μm

In general, aerosol sizes range from a few nanometers to tens of micrometers, (see Figure 3.1 [Watson and Chow, 1999]). Anything smaller than a few nanometers will be considered to be a molecule, i.e., N_2, O_2, etc. Although molecules do have an effect on the electro-optical properties of the atmosphere, their effect is small compared with that of aerosols and can be easily taken into account. Particles >2.5 μm will be considered coarse mode aerosols, which tend to settle out of the atmosphere rather quickly, see Figure 3.2. In general, coarse mode aerosols have only local sources and effects, i.e., near highways or industrial plants, unless coarse mode particulate matter (PM) is transported into the upper atmosphere by volcanic eruptions or other such events. The analysis of the data used in Chapter 4 focuses on ultrafine and fine aerosols, although the data contains information from all size modes.

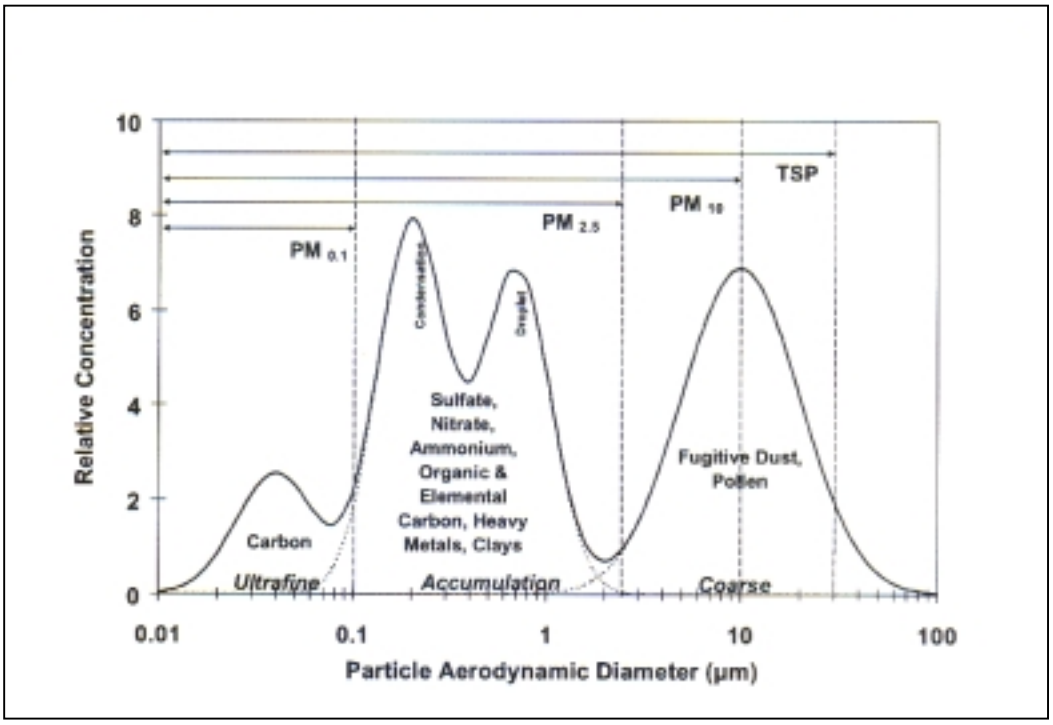

Figure 3.1. Aerosol and particulate distribution: Ultrafine, Accumulation and Coarse [Watson and Chow, 1999].

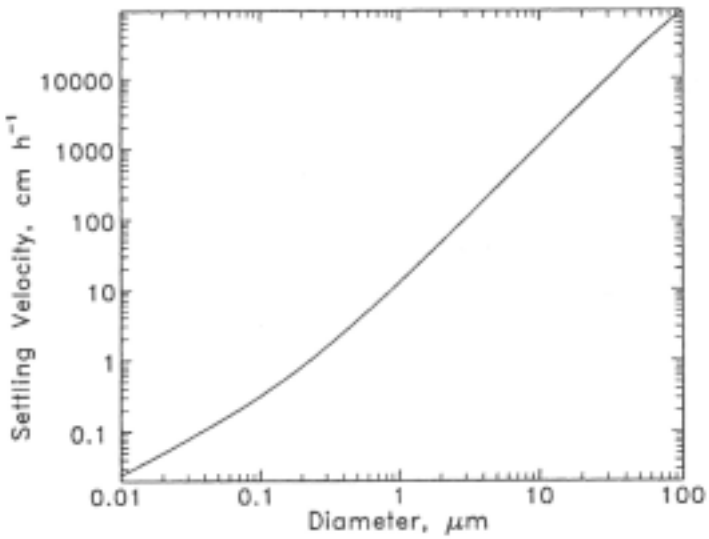

Figure 3.2 Particle setting rate [Seinfeld and Pandis, 1998].

Aerosols can also change their size and composition through condensation, coagulation, chemical reaction, and activation. Condensation occurs when a particle accumulates a vapor species and thereby increases in size, or evaporates a vapor species and decreases in size. Coagulation occurs when particles impact one another and join together forming a larger particle. Chemical reactions between vapors, gases, and/or solids may cause the formation of a new solid particle. Activation occurs when the atmosphere's relative humidity reaches the deliquescence point and water vapor condenses on an aerosol forming a droplet, and therefore increasing the size of the particle, i.e., fog, haze, or cloud formation [Young, 1993]. All of these processes require the initial presence of an aerosol, molecule, or gas that has been entrained in the atmosphere by some source. Further information on aerosol dynamics can be found in Seinfeld and Pandis [1998].

3.2.2 Sources and Compositions

Aerosols are produced at the Earth's surface or within the atmosphere. Surface sources include marine, crustal, biomass, volcano, and anthropogenic materials. Atmospheric sources include clouds and gas-to-particle reactions [Seinfeld and Pandis, 1998].

- Marine sources include sea spray from turbulent water and sea salts from oceanic evaporation. Aerosols generated are mostly composed of water coated sea-salt and dimethylsulfide (CH_3SCH_3) from biogenic oceanic processes [Gabric et al., 1993].

- Crustal sources are mainly deserts, mountains, and cultivated and uncultivated fields. Dust particles are generated and entrained by wind erosion.
- Biomass sources are from plant emission of volatile oils and natural fires. Biological aerosols include nitrates (NO_x), organic carbon (VOC), and fly ash [Hobbs, 1993].
- Volcanic sources can inject massive amounts of particulates into the upper atmosphere that can stay entrained for many years, but will eventually settle out through the lower atmosphere. Materials injected primarily include dust and sulfates (SO_2), which generate acidic aerosols [Hobbs, 1993].
- Anthropogenic sources are introduced into the atmosphere by humans. Sources include industrial processes, non-industrial sources such as roadways, farming, and construction; and transportation sources such as engines, tires, and brakes. Some of the aerosols generated include sulfates, ammonium, nitrates, sodium chloride, trace metals, lead halides, asbestos, crustal elements, water vapor, and carbonaceous materials such as black carbon, graphite, soot, and organic carbon [Hobbs, 1993].
- Cloud sources of aerosols are due the condensation and evaporation processes that form clouds. An aerosol's diameter will increase and its composition can change during cloud condensation. If evaporation processes occur before the aerosol becomes a rain drop, it can stay entrained within the atmosphere [Hobbs, 1993].
- Gas-to-particle sources of aerosols occur due to chemical reactions that grow from molecules and molecular clusters within the atmosphere. Most gas-to-

particle reactions are hygroscopic, and those that are not can be either hetero- or homogeneous chemical reactions [Hobbs, 1993].

3.2.3 Aerosol Removal

Aerosols can have atmospheric lifetimes that range from minutes to decades. The removal of aerosols from the atmosphere mainly occurs by either dry or wet deposition, see Figure 3.3 [Whitby and Cantrell, 1976]. Dry deposition occurs when the particle is either initially too heavy or becomes too heavy through coagulation and the aerosol falls out of the atmosphere. Wet deposition occurs when condensation and nucleation cause's particles to grow by accumulating more water vapor until the particles are too heavy to stay aloft.

As stated in Section 3.2.1, primary and secondary aerosols each have been grouped into 3 modes [Seinfeld and Pandis, 1998]. The particle number concentrations within each mode can fluctuate without wet or dry deposition occurring. Through coagulation and condensation of vapors, nuclei particles can move to the accumulation mode, while cloud processes can move accumulation mode particles to coarse mode [Seinfeld and Pandis, 1998]. Cloud processes can subdivide the accumulation mode into two separate modes, the condensation and droplet modes, see accumulation mode in Figure 3.1 [Watson and Chow, 1999]. The condensation mode occurs as water vapor adheres to aerosols, while the droplet mode occurs when the relative humidity reaches the super saturation level and a droplet is formed.

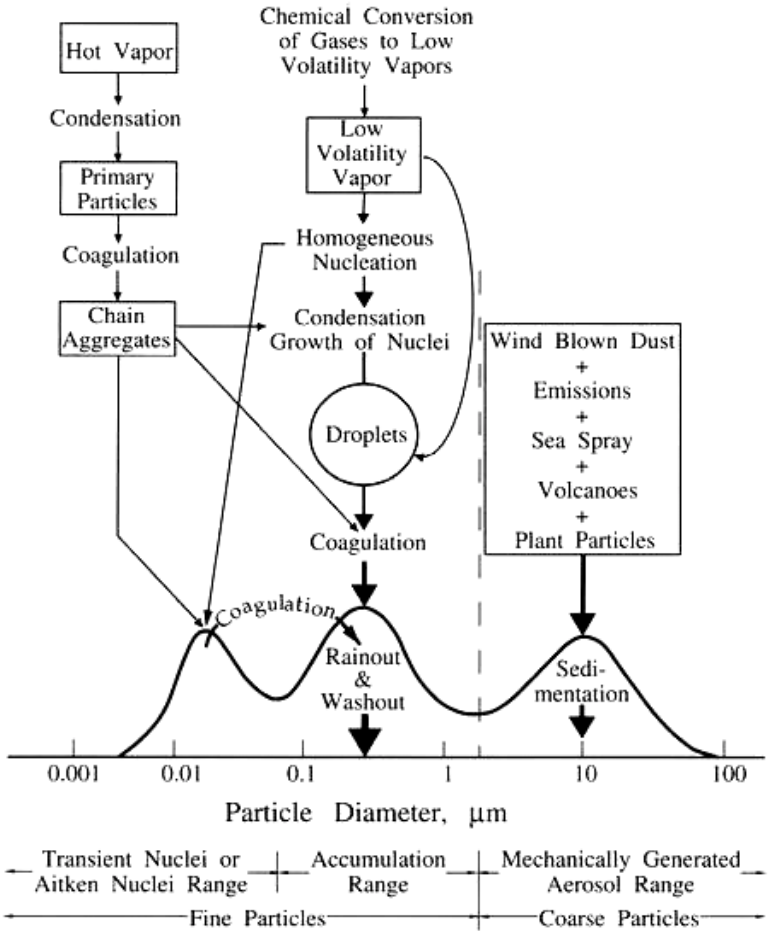

Figure 3.3. Particulate Deposition [Whitby and Cantrell, 1976].

3.3 Water Vapor

Water vapor is a greenhouse gas and is largely concentrated in the lower troposphere. Water vapor, like carbon dioxide and ozone, absorbs IR energy that is re-radiated from the Earth's surface. This absorption of energy by greenhouse gasses is known as the greenhouse effect. Water vapor measurements can serve as a tracer of the dynamics of convective mixing in the lower troposphere [Esposito, 1999]. The sequences of vertical profiles of water vapor can also track advection in the lower

troposphere. The useful information on dynamical processes gained from the water vapor time sequence can also be used to better understand the distribution of aerosols controlled by convection and advection. The presence of high relative humidity can cause aerosol size growth, such as with sulfates which are an abundant east coast pollution aerosol.

3.4 Climate Effects

Earth's climate is a balance between natural heating and cooling, but aerosols and greenhouse gases upset the balance [Seinfeld and Pandis, 1998]. The Earth is primarily warmed by the visible spectrum from the sun and cooled by the reradiating of infrared energy back into space. As discussed in Chapter 2, electromagnetic waves are scattered or absorbed by aerosols, therefore, aerosols can have a large effect on regional and global climates. Aerosols absorb solar radiation and can scatter a portion back into space. Radiating excess heat as IR energy cools the Earth's surface, but aerosols can absorb or re-radiate this energy back to the surface.

Water vapor is the dominate greenhouse gas and accounts for approximately 60-70% of natural greenhouse warming [Schoerer, 2002]. Greenhouse gases add about 2.5 W/m^2 of heat energy to the surface while sulfate and biomass aerosols subtract about 0.5-2.0 W/m^2 [Seinfeld and Pandis, 1998]. Greenhouse gases tend to be uniformly distributed around the Earth and affect the climate during the day and at night. Aerosols, on the other hand, tend to be regionally located, vary with time, are chemically active only during the day and are complicated by meteorology [Seinfeld and Pandis, 1998].

Greenhouse gases also tend to have atmospheric lifetimes on the order of decades to centuries while aerosols tend to be on the order minutes to decades.

Natural meteorological cycles, such as cloud cycles, also have a synergistic effect with aerosols on the climate. If the density of cloud condensation nuclei (aerosols) increases, more clouds can be formed with an associated increase in droplets. The droplets will have small initial diameters that lead to cloud formation with increased albedo [O'Marr et al., 2001].

3.5 Visual Effects

In the previous section, it was stated that aerosols will scatter solar radiation back into space and surface radiation back to the surface. Aerosols also have an effect on visual acuity within the atmosphere.

As stated, aerosols scatter light in all directions and can absorb radiation at selected wavelengths. This leads to a decrease in visibility as aerosols scatter the light between an observer and an object, see Figure 3.4. Light rays between the object and observer's line of sight can be scattered or absorbed, or rays from outside the line of sight can be scattered into the observer's line of sight. This decrease in visibility is actually a reduction in the contrast between the object and the background sky [Seinfeld and Pandis, 1998]. The visual range, or meteorological visibility, is defined as the range at which definition of an object is lost because the light from the object only contributes 2% of the total light observed from the path [Measures, 1984].

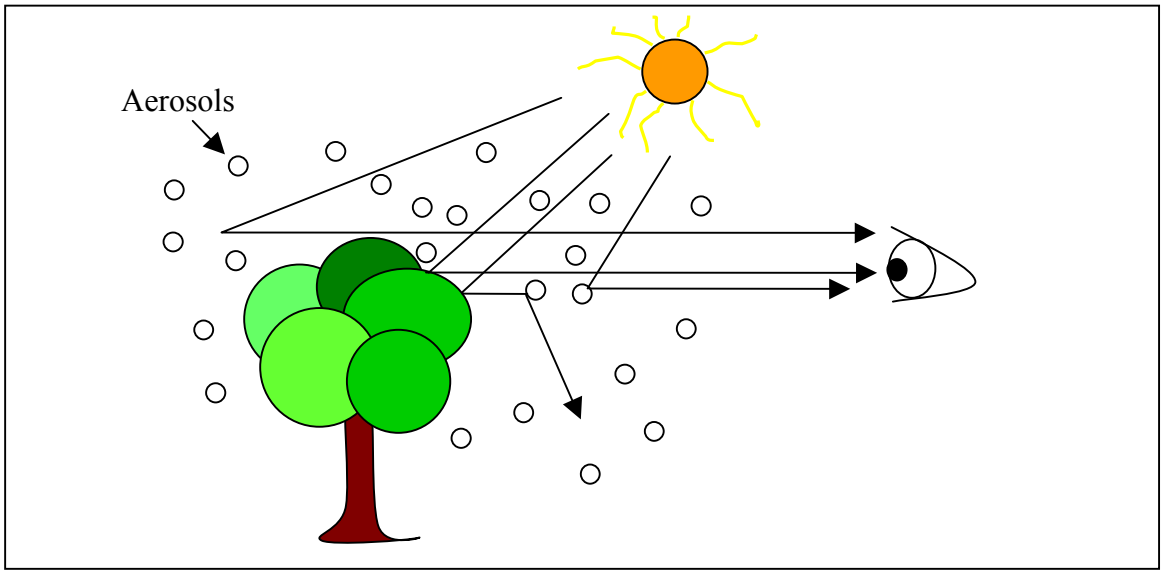

Figure 3.4. Visual and contrast reduction from aerosols scattering light into and out of an observer's line of sight.

Fine and coarse mode particles, 0.1-10 μm in diameter, are the largest cause of visibility reduction [Novitsky, 2002]. Smaller particles, in the ultrafine mode, also contribute to visual reduction by scattering shorter wavelengths. Based on particle composition, graphite carbon is the most abundant light-absorbing aerosol species in the atmosphere [Seinfeld and Pandis, 1998].

3.6 Health Effects

Aerosols not only affect the climatic and visual environments but they also affect humans. Aerosols can severely affect the human respiratory system. The lungs take in the air which humans breathe and absorb oxygen through lung tissue. Aerosols in the 0.001-0.1 μm diameter range are also inhaled with the air and can be deposited in the lungs [EPA, 2002a]. The smaller the aerosol sizes, the deeper into the lungs the particle can be entrenched, which means that fine and ultrafine particles are the largest problems,

see Figure 3.5. Many studies have analyzed the effects that aerosols have on the human respiratory system. The results of these studies suggest that aerosols are a leading cause of increases in human health problems [Hidy et al., 1998]. Aerosols have been linked to increased premature mortality in the elderly and those affected with chronic bronchitis, childhood asthma, asthma requiring hospitalization, heart and lung disease, emphysema, and decreased lung capacity [Hidy et al., 1998; EPA, 2002a; EPA, 2002b].

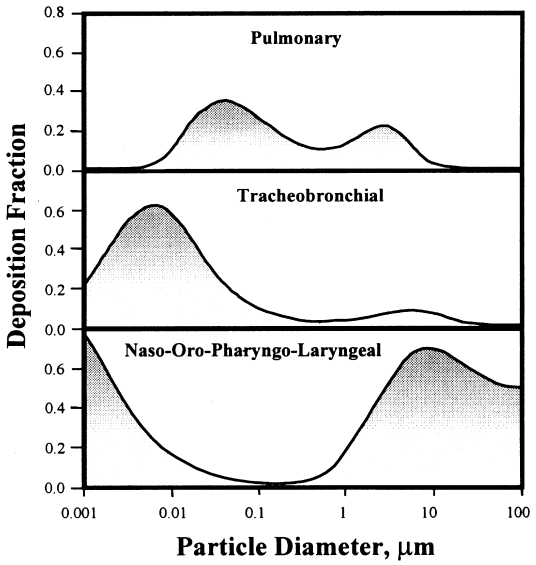

Figure 3.5. Fractional deposition in various regions of the respiratory system as a function of particle size for an average adult male [PM Measurement Workshop, 1998].

Studies have shown that children are being affected greatly by aerosols, since children tend to be more active outside than adults and their respiratory system tissue is more susceptible during development [EPA, 2002a]. Doctors have noted an increase in the numbers of new cases of asthma, especially in children. Aerosols are not only believed to be one of the causes of asthma but also lead to increases in asthmatic attacks and hospitalizations [EPA, 2002b].

Chapter 4

Atmospheric Data Analysis

4.1 Introduction

Optical scattering by aerosols within the lower troposphere are analyzed in this chapter. Analysis of time-sequenced lidar data also provides insight regarding urban pollution episodes. The data sets for this chapter were gathered during North American Research Strategy for Tropospheric Ozone – North East – Oxidant and Particle Study (NARSTO-NE-OPS) summer campaigns in 1998, 1999, and 2001. NARSTO is a public and private organization that facilitates and provides oversight for research activities in Mexico, Canada, and the United States that investigate air pollution episodes. The NE-OPS research site is located northeast of Philadelphia, Pennsylvania. A consortium of universities and government laboratories are involved in the summer campaigns and selected parts of their data will be used to support conclusions drawn. Table 4.1 summarizes the groups and the type of data used during the investigations.

Table 4.1. NARSTO-NE-OPS groups and their data type.

Group	Campaigns	Instrument	Data Used
Millersville University	2001	DustTrac	Balloon PM2.5 mass and RH
Harvard University - SPH	1998 and 1999	TEOM	Ground PM2.5 mass

4.2 Data Explanation

The Penn State LAPS vertical profile data was integrated and stored as raw data files in 1-minute intervals. The raw data files are processed by integrating measured signals for 30-minutes and then stepping forward in the data by 5 minutes to perform a sliding fit. This process is repeated for a specific time sequence interval, usually 6-12 hours in length. The PCount data is integrated and stored in 1-minute intervals and plotted in 1-minute intervals. The MPL data was integrated and stored in 1-minute intervals and plotted with 30-minute integration and 1-minute steps. Finally the MAPP data is a vertical snapshot of the atmosphere and is for the given time instant.

The plots in this chapter depict airborne aerosol in the lower troposphere on 19-22 August 1998; 07, 12, 16 and 17 August 1999; and 23 July 2001 in Philadelphia. All times and dates are presented in UTC time standard, except the MAPP data which uses EST time and UTC dating to avoid jumps in the date stamps during the nighttime data runs. The analysis in this chapter considers particulate matter and water vapor to be aerosols.

During the periods selected for analysis backscatter and extinction levels can be seen to rise as aerosols and water vapor are transported into the area. Backscatter plots will show overall characteristics of the atmosphere, water vapor plots.show changes in the water vapor distribution that can be used to describe dynamical processes Extinction plots at 284- and 530-nm wavelengths illustrate optical characteristics at visible and ultraviolet wavelengths, which can be used to indicate changes in aerosol size.

By using the lidar data and the data of other particulate measurement instruments, atmospheric aerosols can be characterized. Analysis of the lidar data will show that regions of well-mixed aerosols and dense regions of aerosols are detectable. Also, by using multiple wavelengths for extinction coefficient calculation, aerosol mode classifications can be discerned. To show these results LAPS water vapor and extinction, PCount, MPL, MAPP, and instruments that measure particle mass are compared.

4.3 22 August 1998 Analysis

The first set of comparisons are for 22 August 1998 and include time sequences of LAPS water vapor, 284 and 530 nm extinction, MPL vertical profiles and PM2.5 mass measurements. Figure 4.9 depicts a time sequence of water vapor profiles in the lower troposphere. The sun has set before the start of the plot, but the planetary boundary layer (PBL) can be seen to develop below 500 m between 00:00-06:00 UTC. The top of the residual boundary layer remains between 1.0-1.5 km, and can be seen as region of high water vapor in Figures 4.9 and a region of high backscatter coefficient in Figure 4.14. In Figure 4.6, 284 nm extinction shows ultrafine aerosols in the lower troposphere, that corresponds with regions of high water vapor, see Figure 4.9. Since the 530 nm extinction, see Figure 4.7, only shows high extinction coefficients for higher altitude regions; then the regions of high water vapor and ultrafine aerosols in Figures 4.9 and 4.6, respectively, must correspond to haze. This is a reasonable conclusion, since haze generally contains aerosols with diameters < 1 μm. The Micro Pulse Lidar, see Figure

4.14, also shows the nighttime PBL as a region of high backscatter coefficients from 0-500 m and the top of the residual boundary layer between 1.5-2 km. Harvard University-SPH TEOM PM2.5 1-hour mass measurements, see Figure 4.15, show ground particulate matter < 2.5 μm in diameter increasing up to and peaking on 22 August.

a)

b)

c)

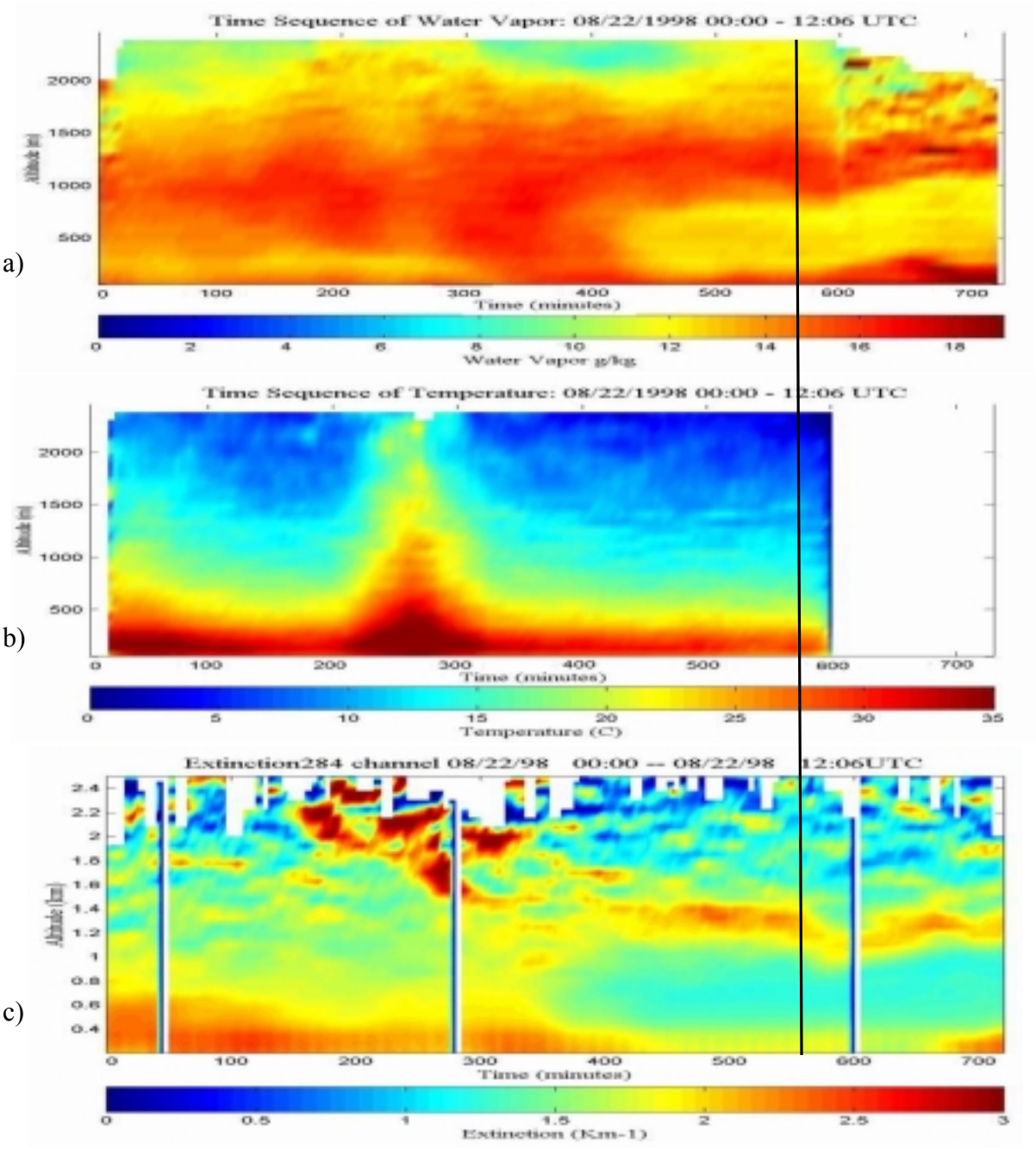

Figure 4.1. LAPS time-sequence plots on 22 August 1998 for: a) water vapor mixing ratio showing the nigttime PBL and the residual daytime PBL; b) temperature showing an increase in temperature at approximately minute 275; and c) 284-nm extinction showing good correlation with atmospeheric waper vapor advection and convection and an increase in extinction coefficients corresponding to the temperature increase (approximate time of sunrise is indicated by black line).

a)

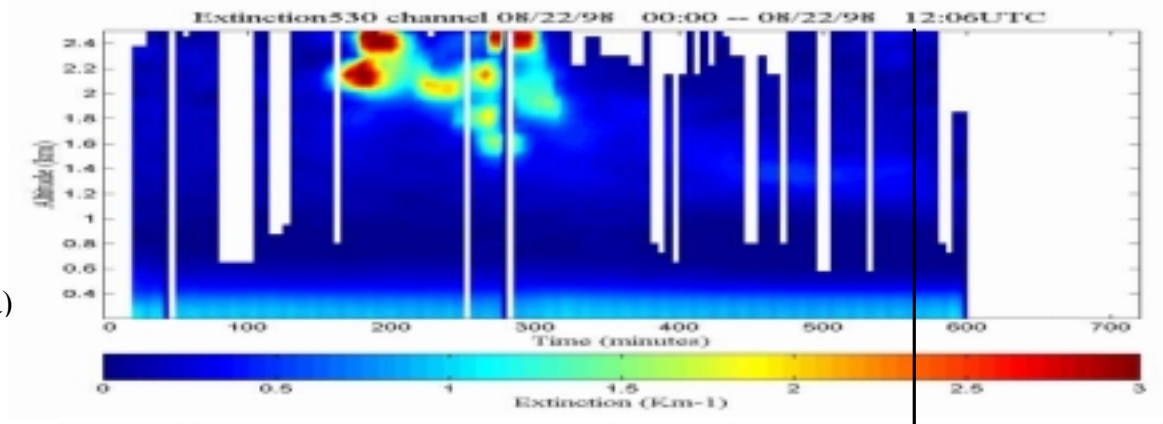

b)

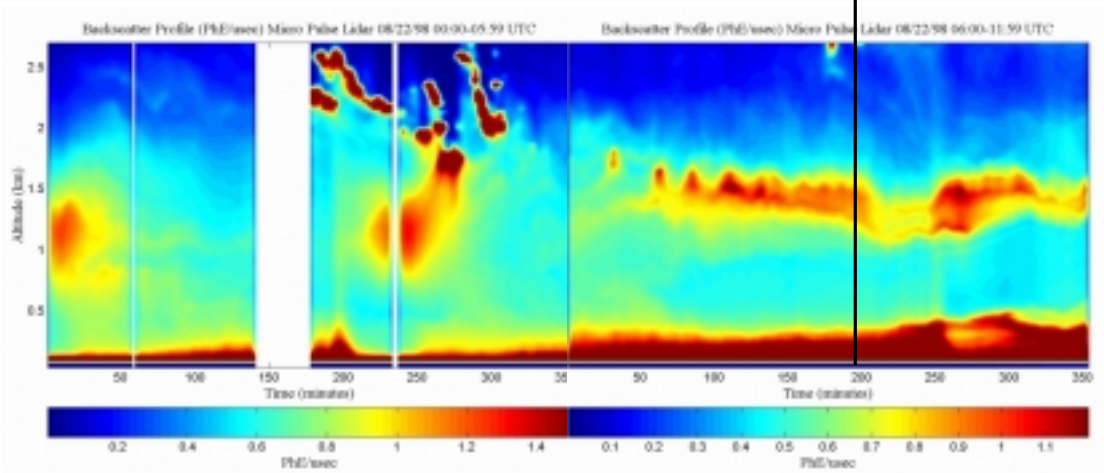

c)

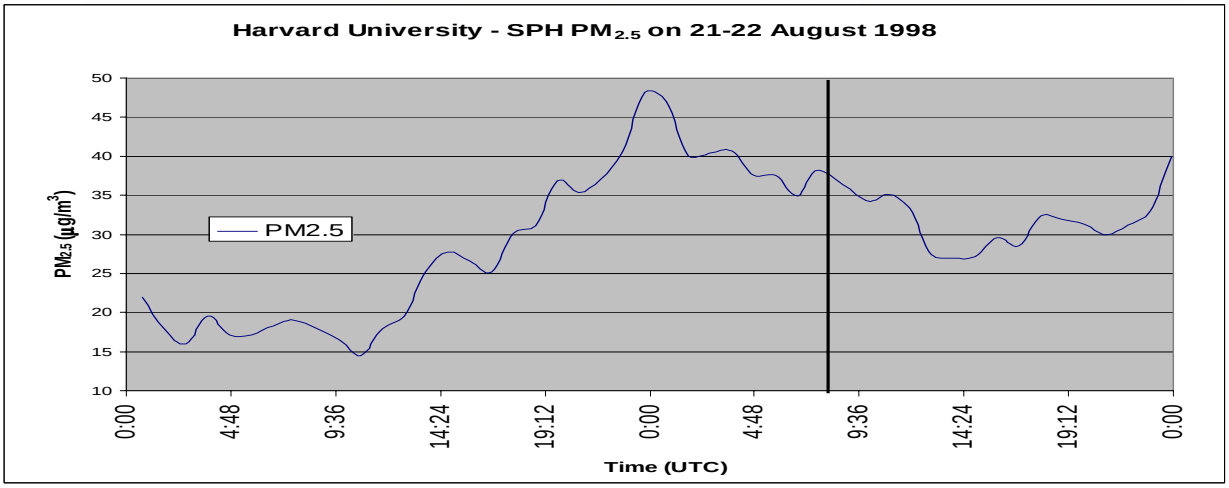

Figure 4.2. Time-sequence plots on 22 August 1998 for: a) LAPS 530-nm extinction showing aerosol growth corresponding to increases in water vapor and temperature; b) MPL backscatter plot showing nighttime PBL and high backscatter coefficients at the residual PBL altitude (1.5 km); and c) Harvard University – SPH PM2.5 mass (approximate time of sunrise is indicated by black line).

4.4 16-17 July 1999 Analysis

During 16-19 July 1999 the northeastern United States experienced what is known as a Haze Event [Poirot, 2002]. Aerosols that had previously been blown out over the Atlantic Ocean were redirected by wind back to the northeast. The aerosol haze remained entrained over the northeastern U.S. from the Chesapeake Bay to Maine, see Figure 4.16.

Figure 4.3. SEAWIFS satellite image of 16-19 July 1999 Northest HAZE Event [Poirot, 2002].

Figure 4.17 shows the relatively constant high water vapor mixing ratio during the Haze Event as a layer from 0-2 km. The top of the nighttime planetary boundary layer can be seen as a red band between 500-1000 m. A band of water vapor can also be seen at ground level. Figures 4.18 and 4.19 contain the time sequences of the 284 and 530 nm extinction profiles, respectively. The 284 nm extinction illustrates the ultrafine aerosols contained in the haze, while the 530 nm extinction shows that a ground layer of fine particles coincides with the band of high water vapor in Figure 4.17 and where the

approximate height of the nighttime planetary boundary layer should be located between 200-300 m.

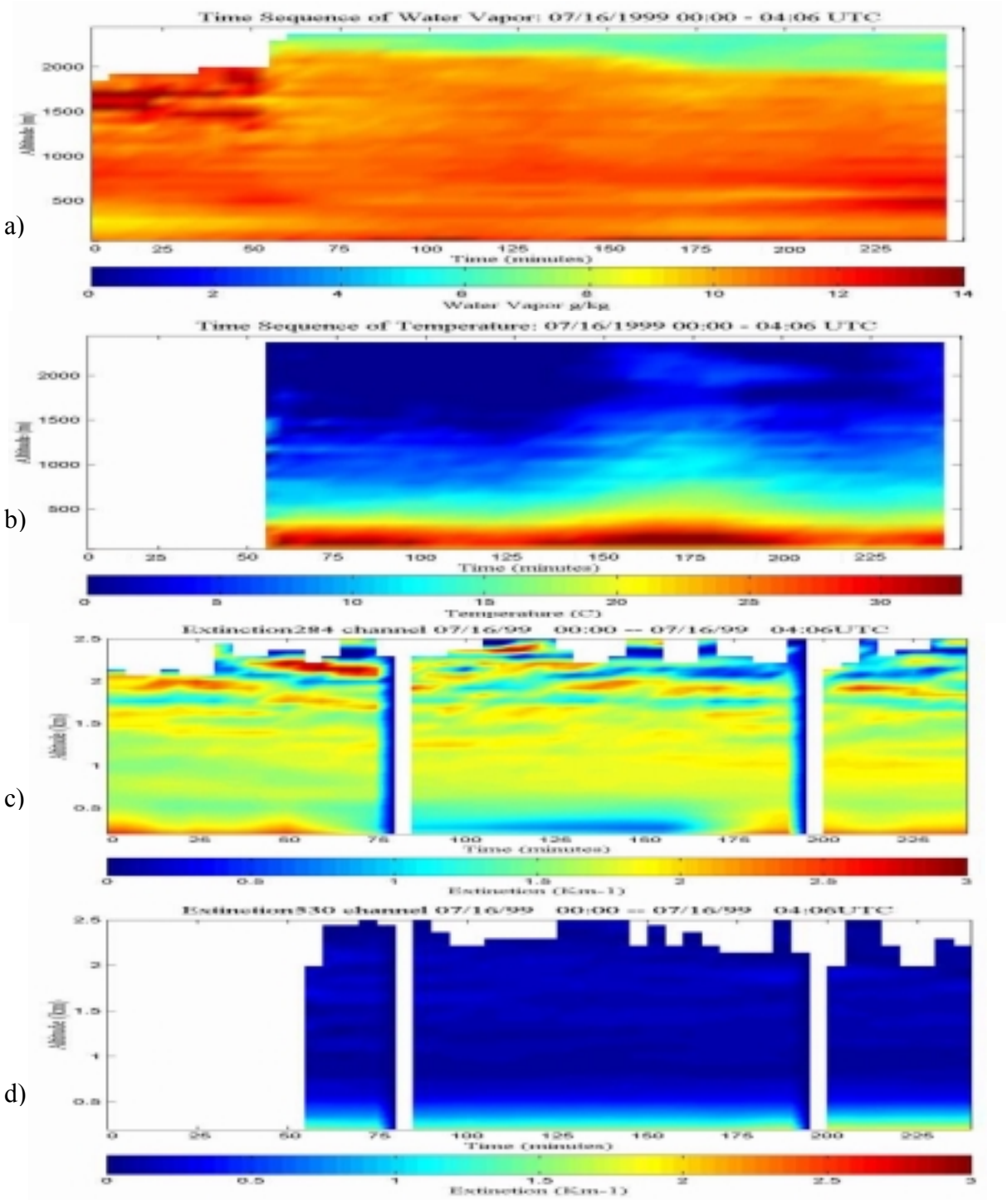

Figure 4.4. LAPS time-sequence plots during Haze Event on 16 July 1999 for: a) water vapor mixing ratio showing water vapor well distributed in the residual PBL; b) temperature showing a steep temperature gradient; c) 284-nm extinction showing a well mixed lower atmoshere with small extinction coefficient gradient for ultrafine and fine mode aerosols; and d) 530-nm showing fine and coarse mode aerosol growth at the surface.

The next sequence of figures contains the water vapor, extinction, and direct backscatter plots for the second day of the Haze Event. The nighttime boundary layer in Figure 4.20 is a band of red at approximately 1000 m and the water vapor has increase from the 16th to the 17th. The ultrafine aerosols have also increased, seen as higher extinction coefficients in Figure 4.21. Also Figures 4.20 and 4.21 have a good correlation with their plotted details; bands at 1000 m and an area of decreased water vapor and extinction at 500 m from 03:00-06:21 UTC. Figure 4.22 shows that the fine aerosols remain the same until about 07:00 UTC when an increase can be seen as higher 530 nm extinction coefficients. Figure 4.23 has three plots from the PCount that show strong direct backscatter between 500-1500 m along with the photon count returns which show a thick return peak between 500-1000 m. Figure 4.24 contains Harvard University-SPH PM2.5 mass measurements for 16-17 July 1999 which show high peaking ground particle mass for particles < 2.5 μm in diameter.

lv

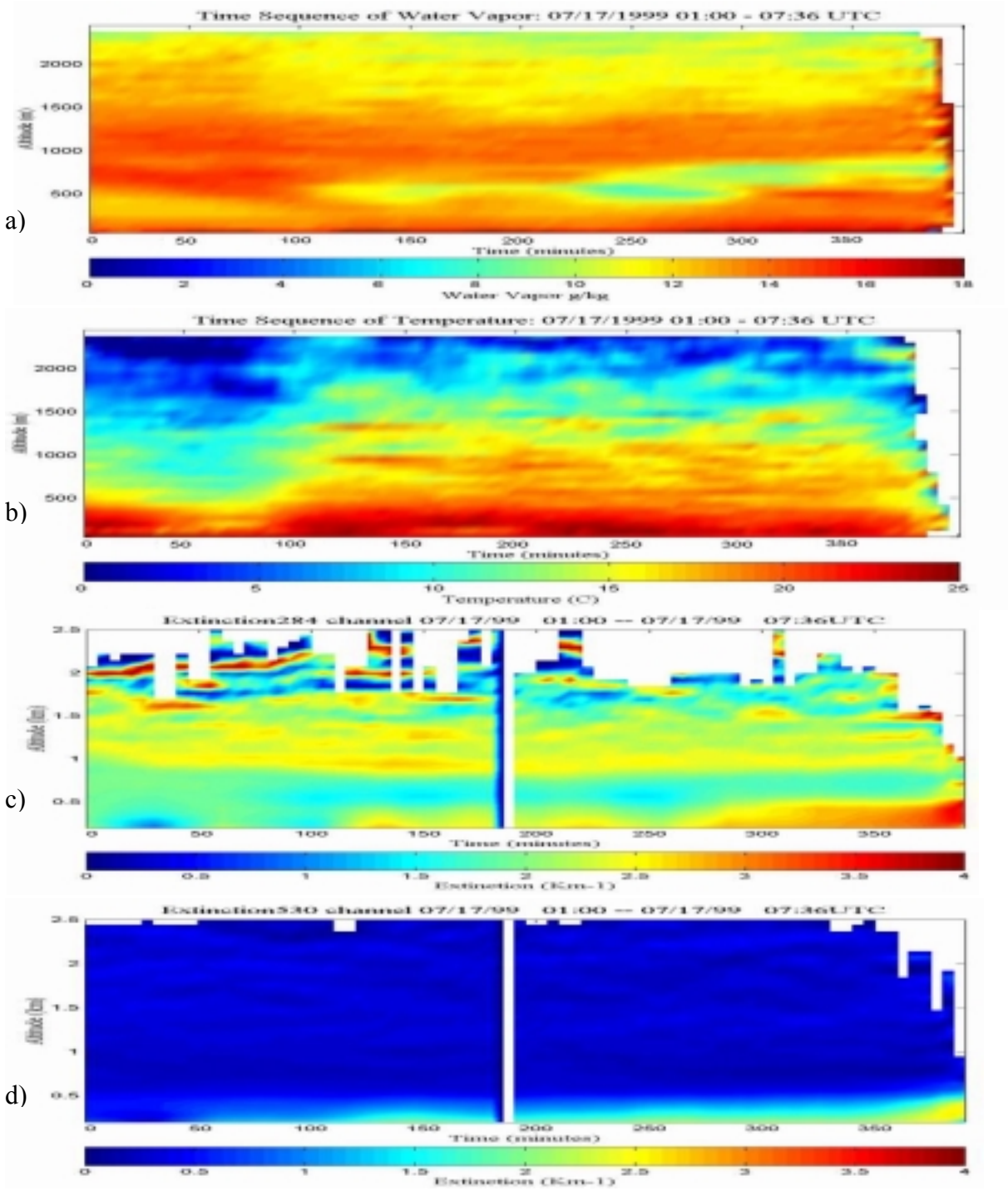

Figure 4.5. LAPS time-sequence plots during Haze Event on 17 July 1999 for: a) water vapor mixing ratio showing an increase in water vapor content from the previous day and water vapor well distributed in the residual PBL; b) temperature showing a more gradual temperature gradient than the pervious day; c) 284-nm extinction showing a well mixed lower atmoshere with a lager extinction coefficient gradient for ultrafine and fine mode aerosols than for 16 July; and d) 530-nm showing a gradual increase in fine and coarse mode aerosol growth at the surface.

lv

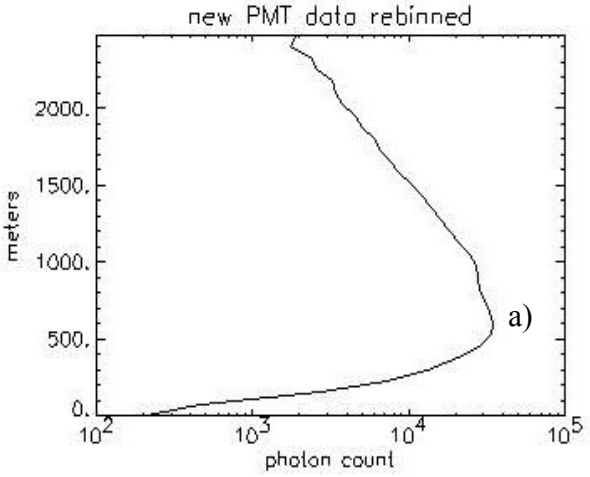
new PMT data rebinned
meters
2000.
1500.
1000.
500.
0.
10^2
10^3
10^4
10^5
photon count

a)

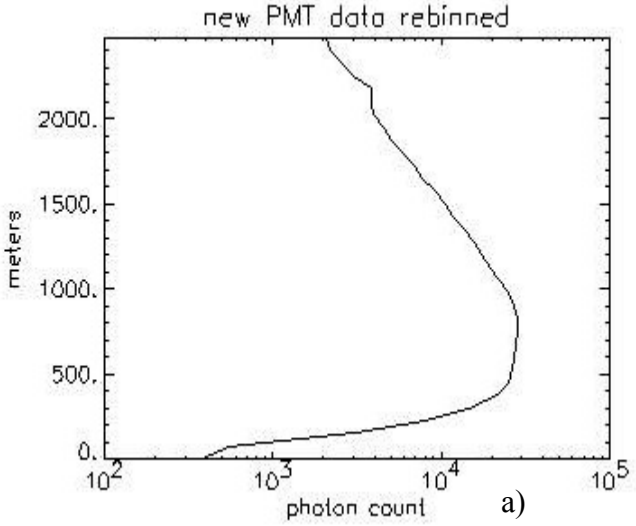
new PMT data rebinned
meters
2000.
1500.
1000.
500.
0.
10^2
10^3
10^4
10^5
photon count

a)

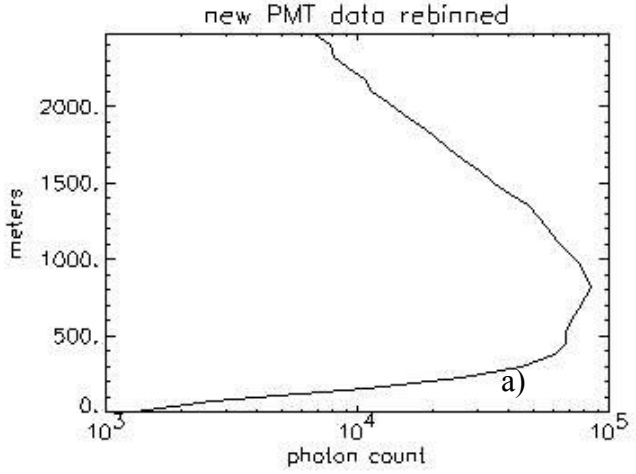
new PMT data rebinned
meters
2000.
1500.
1000.
500.
0.
10^3
10^4
10^5
photon count

a)

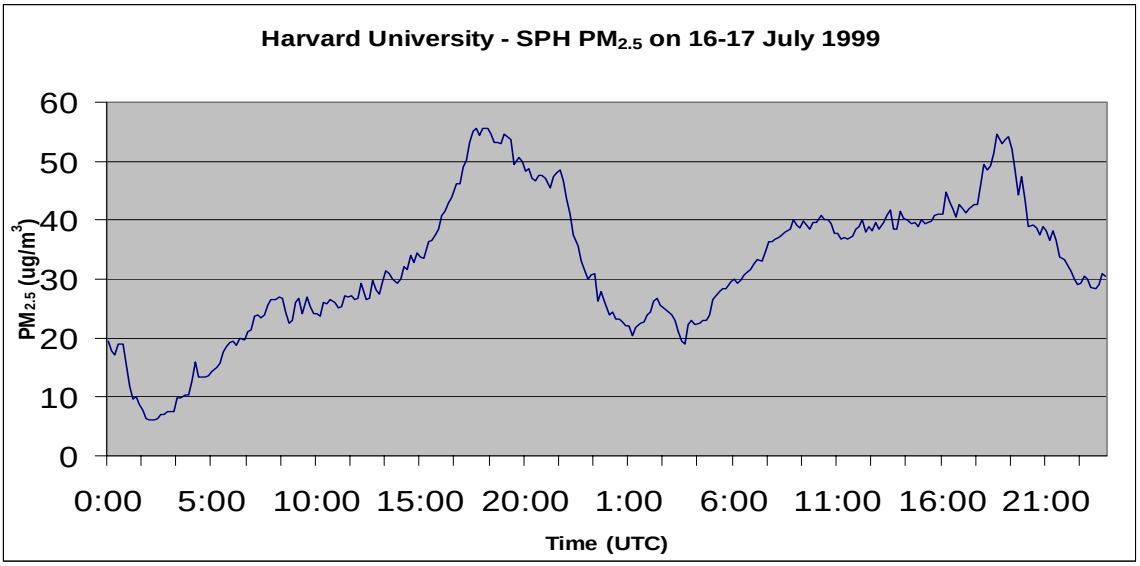

Figure 4.7. Harvard University-SPH $PM_{2.5}$ mass measurements for 16-17 July 1999, showing mass increases, for PM less or equal to 2.5 μm, throughout the day and peaking after sunset on the 16th and 17th.

4.5 23 July 2001 Analysis

The last data set comparison c uses data gathered on 23 July 2001. The time sequence plot of water vapor in Figure 4.25 shows the top of PBL at its nighttime at altitude. A region of high water vapor below 500 m moves into the monitoring area about 07:00 UTC. The 284 nm extinction, Figure 4.26, shows a dense region of ultrafine aerosol extinction occurring around 1 km, whereas the 530 nm extinction plot Figure 4.37 shows a negligible amount of extinction occurring. The extinction bands in Figures 4.26 and 4.27 at 500 m can be neglected as regions of bad data. The form factor calibration for calculating the extinction for the summer 2001 campaign has not been fully solved. In Figures 4.26 and 4.27 and increase in the extinction coefficients occurs between 275-

354 minutes and below 100 m. The increase begins first as an increase in the ultrafine aerosols at minute 275 in Figure 4.26 then proceeds to fine aerosols at about minute 315 in Figure 4.27. The MAPP image of the polarization ratio versus altitude in Figure 4.28 was taken during the increase in extinction below 100 m and has a peak at approximately 40 m. Figure 4.28 has a strong comparison between cameras B and C in both plots, but the data does not overlay in the polarization ratio versus scattering angle plot. The shift in the data between camera B and C shows that the scattering detected by the cameras is occurring at different altitudes within the peaks in the polarization ratio versus altitude plot. This is due to aerosol layers within the lower troposphere that have been transported into the scattering volume. The Millersville University DustTrac $PM_{2.5}$ data shows a relatively well-mixed atmosphere from 0-200 m, while the MAPP data demonstrates that there are variations within the first 40 m. The tethered balloon took samples at 0, 100, 200 and 300m, where as the MAPP has range bins increasing from 0.015-1 m for the first 100 m of the atmosphere. Millersville University's relative humidity measurements also peak at approximately the same time that Figure 4.25 shows a high water vapor mixing ratio return between 06:30-8:55 UTC and below 500 m.

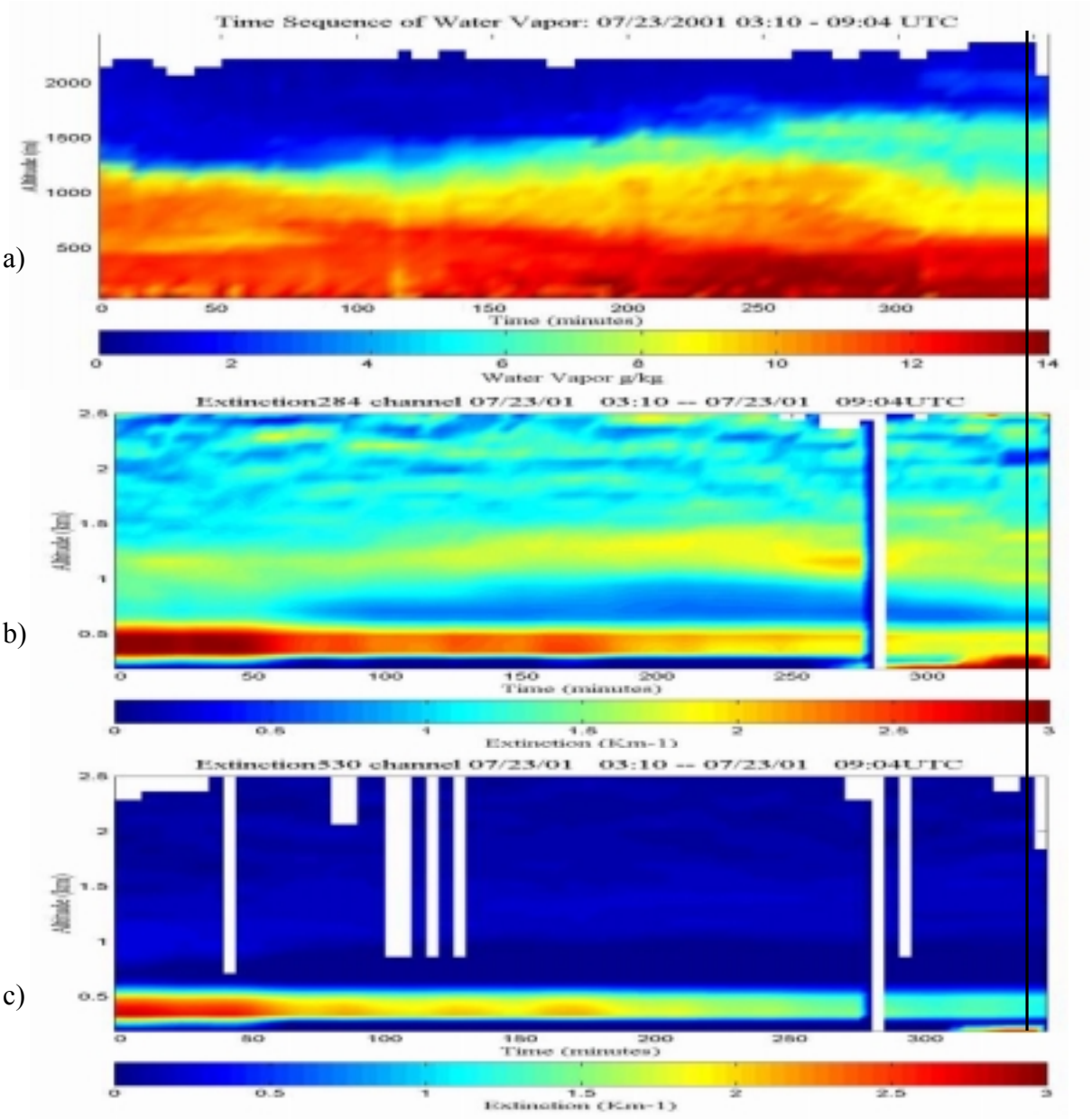

Figure 4.8. LAPS time-sequence plots on 23 July 2001 for: a) water vapor mixing ratio showing showing the nigttime PBL and the residual daytime PBL; b) 284-nm extinction showing a mixed lower atmoshere with an extinction coefficient gradient for ultrafine and fine mode aerosols at 1 km and a steep extinction coefficient gradient corresponding to ultrafine and fine mode aerosol growth below 200 m starting at minute 275; and d) 530-nm extinction showing negligible extinction coefficients above 500 m, and fine and coarse mode aerosol growth below 100 m

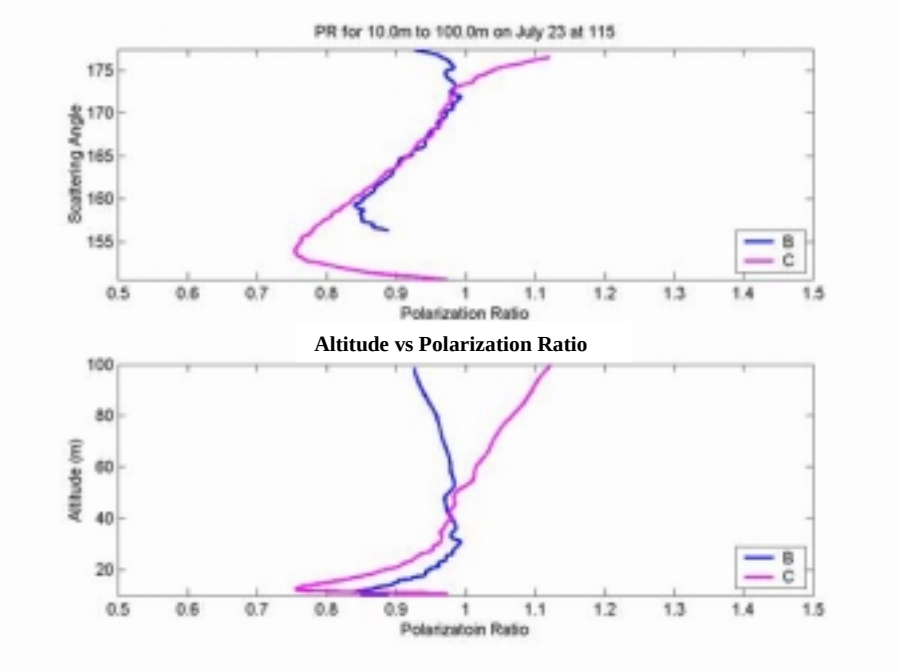

Figure 4.11. MAPP plot for 23 July 2001 at 01:15 EST.

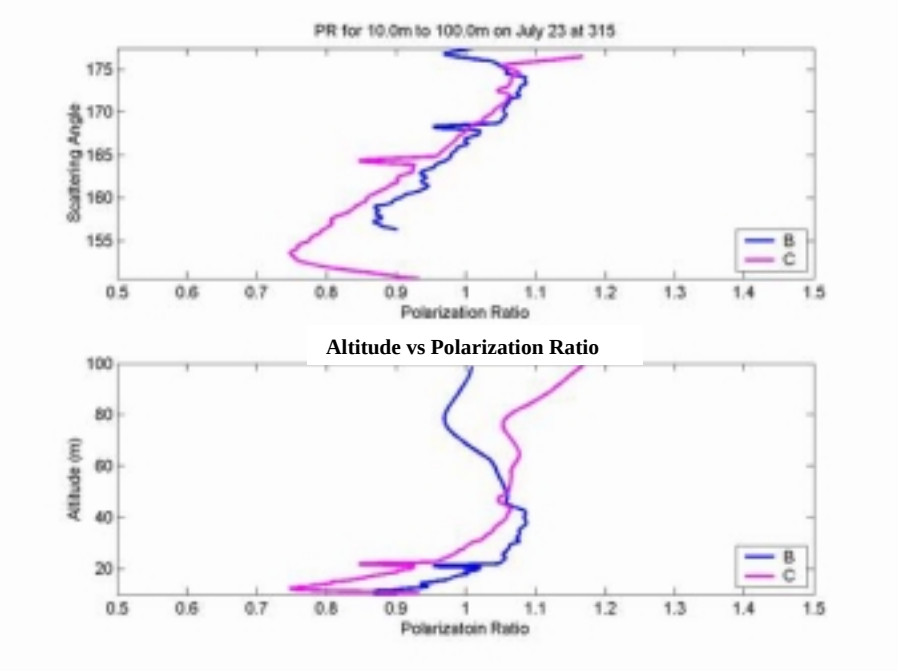

Figure 4.28. MAPP plot for 03:15 EST 23 July 2001 showing aerosol layers between 20-40 m.

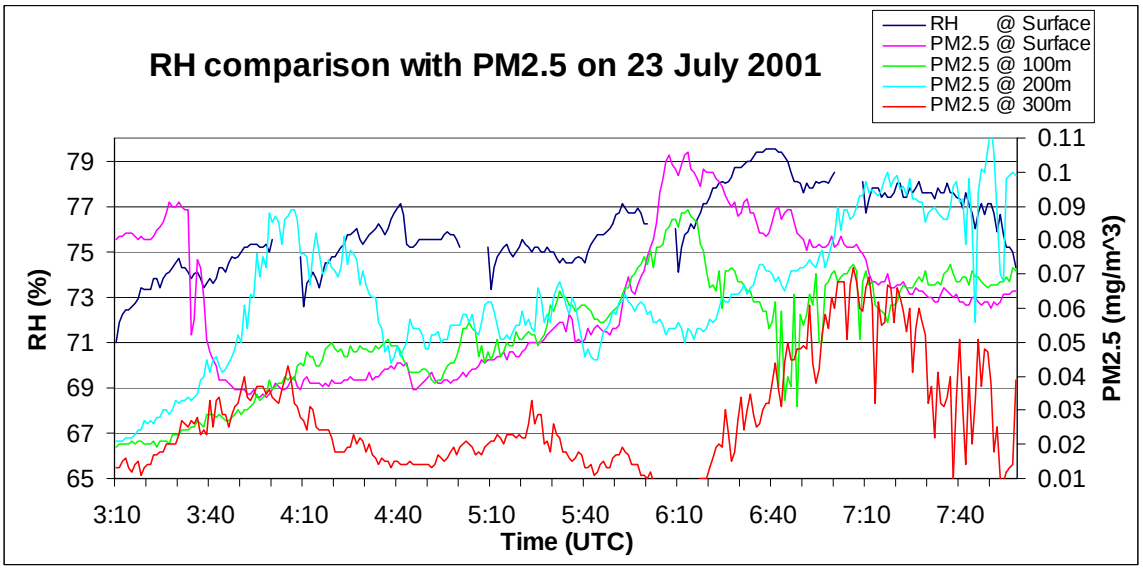

Figure 4.10. Millersville University relative humidity and tethered balloon $PM_{2.5}$ DustTrac mass measurement for 23 July 2001.

Chapter 5

Conclusions

As humans change their surrounding environment, pollution studies are and will become increasingly important to governmental agencies and private organizations as a way to monitor that change. Studies such as NARSTO - NE - OPS help to develop an understanding of the physical processes and models for air pollution events. These studies also provide an opportunity for universities, industry, and organizations to test new equipment and monitoring units.

By analyzing data taken during each summer campaign and then making comparisons between different collection periods it is possible to gain a clear understanding of the necessary data analysis techniques. In the case of the Penn State University's LAPS instrument, it allows comparisons to be made between each summer's data set as the unit is modified and upgraded. These studies also provide an arena for the exchange of data between groups who have taken data at the same time and location.

Analysis of LAPS, MPL, and MAPP data has shown that lidar can monitor the advection and convection of aerosols that lead to pollution events [Mulik, 2000; Esposito, 1999; Li, 2000]. Time-sequence plots of extinction are able to show airborne aerosol distribution, which can be uniformly well mixed or spatially dense. By comparing 284- and 530-nm extinction, aerosol mode approximations can be made since ultrafine and fine particles will cause strong 284-nm extinction while fine and larger particles will affect the 530-nm channel. Then, by using time sequence plots of the water vapor mixing

ratio, regions of high water vapor can be discerned. Water vapor and optical extinction plots can also show regions where condensation growth of particles is occurring. Condensation growth of particles causes aerosols to increase in diameter, as can be seen by comparing 284- and 530-nm extinction coefficients, and occurs in regions of high water vapor. Water vapor plots can be used to follow variations of the planetary boundary layer and convective mixing within the lower troposphere, which leads to the transportation of aerosols in the lower troposphere. The Micro Pulse Lidar and PCount provide information on the direct backscatter of atmospheric aerosols. By looking at direct backscatter plots, the regions of higher densities of particles will show stronger returns and photon-count-versus-altitude plots show the distinct altitude of the dense regions and how thick they are. The Multistatic Atmospheric Particle Profiler can discern aerosol layering and size distribution within the first 100 m of the troposphere. The polarization-ratio-versus-altitude plots provide information on regions containing high scattering volumes. By comparing the polarization ratio versus altitude with the polarization ratio versus scattering angle it is possible to see if the scattering volumes are at the same altitude or if there are several scattering layers.

The composition and movements of the atmosphere can change rapidly or slowly, be mixing or stagnant, and be calm or disturbed; for these reasons monitoring instruments need to have sufficient time and space resolution to follow the variations of the properties. Besides being accurate, data must be taken frequently. Laser remote sensors such as LAPS allow continuous accurate monitoring achievable. By making intercomparisons of summer campaigns and using several monitoring instruments, their

limitations can be found and improvements in their data collecting ability can be made. LAPS' PCount channel demonstrates that the photon counting electronics need upgrading from 500-ns bin widths to 20-ns, which provide 3-m resolution instead of the current 75-m resolution. This upgrade will lead to being able to see more detail of the aerosol structure of the lower troposphere. The Multistatic Atmospheric Particle Profiler is a new instrument and still being developed. A detailed analysis of the algorithms involved in data processing will need to be formed. The bulk processing capabilities have been developed but the calibration constants and fine tuning of the algorithms will have to be accomplished before MAPP data will be accurate on a regular basis and usable with an unknown atmosphere.

At present, the Penn State University LAPS instrument is able to monitor on a semi-continuous basis. The LAPS unit provides data on large meteorological structures of the lower troposphere. Water vapor mixing ratio provides data on water vapor movement, which has been linked to pollution transport [Esposito, 1999]. Extinction channels can show atmospheric extinction caused by airborne aerosols. By looking at each of the 284, 530, and 607 nm channels, an aerosol mode range for the extinction causing aerosols can be discerned as the extinction gradient changes [Schuster et al., 1998]. The MAPP instrument can show the layering of lower tropospheric aerosols. The PCount channel can be used to make intercomparisons between the water vapor and extinction channels by showing regions of high backscatter coefficients. The comparisons between all the lidar units and supported by other groups has shown that

airborne aerosols can be detected within the lower troposphere and that an aerosol mode range can be approximated for the aerosols involved.

REFERENCES

Ansmann, A., U. Wandinger, M. Riebesell, C. Weitkamp and W. Michaelis, "Independent Measurement of Extinction and Backscatter Profiles in Cirrus Clouds by Using a Combined Raman Elastic-Backscatter Lidar," *Applied Optics*, Vol. 31, No. 33, pp. 7113 - 7131, 1992.

Anthes, R.A., H.A. Panofsky, J.J. Cahir and A. Rango, The Atmosphere, Bell and Howell, Ohio, 1975.

Bohren, C.F. and D.R. Huffman, Absorption and Scattering of Light by Small Particles, John Wiley and Sons, New York, 1983.

Chadha, Ginnipal S., "Optical Design for Advanced Lidar Detectors," Master of Science Thesis for Penn State University, Department of Electrical Engineering, May 2001.

Environmental Protection Agency (EPA, 2002a, March), Health and Environmental Effects of Particlulate Matter [WWW document].
URL: http://www.epa.gov/ttn/oarpg/naaqsfin/pmhealth.html

Environmental Protection Agency (EPA, 2002b, March), Human Health Benefits from Sulfate Reduction Under Title IV of the 1990 Clean Air Act Amendments [WWW document].
URL: http://www.epa.gov/airmarkt/articles/healtheffects/huhealth.pdf

Esposito, Steven T., "Applications and Analysis of Raman Lidar Techniques for Measurements of Ozone and Water Vapor in the Troposphere," Master of Science Thesis for Penn State University, Department of Electrical Engineering, May, 1999.

Gabric, A., C.N. Murray, L. Stone and M. Kohl, "Modelling the Production of Dimethylsulphide During a Phytoplankton Boom," *Journal of Geophysical Reseach*, Vol. 98, C12, 22805 - 22816, 1993.

Hecht, Eugene, Optics, Addison Wesley, Boston, 3rd Edition, 1997.

Hidy, G.M., P.M. Roth, J.M. Hales and R. Scheffe, "Oxidant Pollution and Fine Particles: Issues and Needs," North American Research Strategy for Tropospheric Ozone, Breifing Package, White Paper, 1998.
URL: ftp://ftp.cgenv.com/pub/downloads/Hidy.pdf

Hlavka, Dennis L., James D. Spinhirne and James R. Campbell, "Aerosol Analysis Techniques and Results from Micro Pulse Lidar," Proceedings of the 19th International Laser Radar Conference, NASA Langley Research Center, pp. 155 - 163, July 1998.

Hobbs, P.V., Aerosol – Cloud - Climate Interactions, Academic Press, Inc., 1993.

Institute on Climate and Planets (ICP, 2002, March). How Do Aerosols Affect Earth's Climate and Our Health? [WWW document].
URL: http://icp.giss.nasa.gov/outreach/newsletter/v3i1/rsedv3i1_aerosols.pdf

Jeness, J.R., D.B. Lysak, Jr. and C.R. Philbrick, "Design of a Lidar Receiver with Fiber-Optic Output," *Applied Optics*, Vol. 36, No. 18, pp. 4278 - 4284, 1997.

Kyle, T.G., Atmospheric Transmission: Emission and Scattering, Pergamon Press, New York, 1991.

Lee, H.S., I.H. Hwang, J.D. Spinhirne and V.S. Scott, "Micro Pulse Lidar for Aerosol and Cloud Measurement," Selected Papers of the 18th International Laser Radar Conference (ILRC), Berlin, pp. 7 - 10, July 1996.

Li, G., G.S. Chadha, K.R. Mulik, and C.R. Philbrick, "Characterization of Properties of Airborne Particlate Matter from Optical Scattering Using Lidar," PM2000, 2000.

Measures, Raymond M., Laser Remote Sensing, Wiley - Interscience, New York, 1984.

Mulik, K.R., G. Li, G.S. Chadha and C.R. Philbrick, "Evolution of Air Polution Events Determined from Rmana Lidar," Proceedings of the A&WMA Specialty Conference and Exhibition, PM2000: Particulate Matter and Health, Charleston, South Carolina, pp. 4ASP2: 11-13, January 24 - 28, 2000.

Mulik, Karoline R., "Evolution of Ozone and Particulate Matter During Pollution Events Using Raman Lidar," Master of Science Thesis for Penn State University, Department of Electrical Engineering, May, 2000.

Novitsky, Edward J., "Multistatic Lidar Profile Measurements of Lower Troposheric Aerosols and Particulate Matter," Doctor of Philosophy Thesis for Penn State University, Department of Electrical Engineering, 2002.

O'Marr, E.E., T.D. Sikora, G.S. Young and R.F. Gasparovic, "Anomalous Cloud Lines Over the Mid-Atlantic Coast of the United States," *Canadian Journal of Remote Sensing*, Vol. 27, No. 4, pp. 320 - 327, 2001

Philbrick, C.R. and D.B. Lysak, "Atmospheric Optical Extinction Measured by Lidar," NATO_RTO Metting Proceedings I, E-O Propagation, Signature and System Performance Under Adverse Meteorological Conditions, Vol. 40, pp. 1 - 7, 1998.

Philbrick, C.R. and K.R. Mulik, "Application of Raman Lidar to Air Quality Measurements," Laser Radar Technology and Applications V, Proceedings of SPIE, Vol. 4035, pp. 22 - 33, April, 2000.

Poirot, Rich, (2002, April). 7/16 - 17/99 Northeast Fine Particle and Ozone "Haze" Episode [WWW document].
URL http://capita.wustl.edu/neardat/Activities/july99/july99.htm

Radke, L.F. and P.V. Hobbs, "Measurement of Cloud Condensation Nuclei, Light Scattering Coefficient, Sodium - Containing Particles, and Aitken Nuclei in the Olympic Mountains of Washington," *Journal of the Atmospheric Sciences*, Vol. 26, No. 2, pp. 281 – 288, 1969.

Rajan, S., T.J. Kane and C.R. Philbrick, "Multiple-wavelength Raman Lidar Measurements of Atmospheric Water Vapor," *Geophysical Research Letters*, Vol. 21, No. 23, pp. 2499 - 2502, 1994.

Schloerer, J., (2002, March). Climate Changes: Some Basics [WWW document].
URL http://www.radix.net/~bobg/faqs/scq.basics.html

Schuster, G.L., S.T. Esposito and C.R. Philbrick, "Optical Extinction in Clouds at Multiple Wavelengths," Proceeding of 19th International Laser Radar Conference, NASA/CP-1998-207671/PT1, pp 193 - 194, 1998.

SESI, Micro Pulse Lidar Instruction Manual, Rev. 2, 1996.

Seinfeld, J.H. and S.N. Pandis, Atmosperic Chemistry and Physics, From Air Pollution to Climate Change, John Wiley and Sons, New York, 1998.

Watson, J.G., and J.C. Chow, Reconciling Urban Fugitive Dust Emissions Inventory and Ambient Source Contribution Estimates: Summary of Current Knowledge and Needed Research, Desert Research Institute, Energy and Environmental Engineering Center, DRI Document No. 6110.4D2, 1999. (DRAFT)

Whitby, K.T. and B. Cantrell, "Fine Particles," International Conference on Environmental Sensing and Assessment, IEEE, Las Vegas, NV, 1976.

Young, K.C., Microphysical Processes in Clouds, Oxford University Press, New York, 1993.